First publ. in: Laser Cleaning / ed. Boris Luk'yanchuk. New Jersey, World Scientific, 2002, pp.103-178

Chapter 3

OPTICAL RESONANCE AND NEAR-FIELD EFFECTS IN DRY LASER CLEANING

B. S. Luk′yanchuk, M. Mosbacher, Y. W. Zheng, H. - J. Münzer,
S. M. Huang, M. Bertsch, W. D. Song, Z. B. Wang, Y. F. Lu,
O. Dubbers, J. Boneberg, P. Leiderer, M. H. Hong, T. C. Chong

Optical problems, related to the particle on the surface, i.e. optical resonance and near-field effects in laser cleaning are discussed. It is shown that the small transparent particle with size by the order of the wavelength may work as a lens in the near-field region. This permits to focus laser radiation into the area with the sizes, smaller than the radiation wavelength. It leads to 3D effects in surface heating and thermal deformation, which influences the mechanisms of the particle removal.

Keywords: Near-field effect, Optical resonance, Modeling, Dry laser cleaning, Threshold, Oscillations, SiO_2 particles, Si.

PACS: 42.62.Cf, 81.65.Cf, 81.07.Wx

1. Introduction

Up to now there is no completely satisfactory industrial solution for the surface cleaning involving submicrometer particles. The technique of laser cleaning, utilizing short-pulsed laser irradiation, sometimes in conjunction with the deposition of a liquid-film on the surface, has been studied and utilized since the late 1980's in several Institutes and R&D Centers (Beklemyshev, 1987; Assendel'ft, 1988 a, b; Kolomenskii, 1991; Zapka, 1991 a; Imen, 1991 a). Around 1990's a few successful examples for microelectronics and data-storage industrial applications were demonstrated (see patents of Zapka, 1989; Boykov, 1991; Imen, 1991 b).

There are two basic mechanisms of laser cleaning: the mechanism, based on evaporation of liquid film is called a "steam" laser cleaning, while laser cleaning without the usage of liquid film is called "dry" laser cleaning. It is considered that thermal expansion effects cause dry laser cleaning.

Previous examinations of the dry laser cleaning were investigated for two particular cases: 1) expansion of absorbing particle on the transparent substrate and 2) expansion (thermal deformation) of the absorbing substrate with non-absorbing particle (Bäuerle, 2000). The mutual influence of the particle and substrate was ignored in this approach. Nevertheless, the latest researches (Luk`yanchuk, 2000; Mosbacher, 2001) show that these feedback effects play an important role and suggest the understanding of dry laser cleaning in somewhat different terms than traditional approach. For example, the material optical properties influence the distribution of absorbed and scattered energy, which can be rather complex. In free space these distributions for the spherical particle can be found from the Mie theory (Born & Wolf, 1999; Barber & Hill, 1990).

As it was shown in the recent publications (Lu, 2000 a, b, c; Leiderer, 2000; Luk'yanchuk, 2000, 2001, 2002 a, b; Mosbacher, 2001, 2002; Zheng, 2001; Münzer, 2001, 2002) the small transparent particle can work as a focusing lens even at the particle size (radius a) comparable with radiation wavelength, λ. If one considers the particle as a perfect sphere, then in the Mie theory a size parameter $q = 2\pi a/\lambda$ appears. As this parameter changes, extinction and other scattering characteristics of the particle show oscillations, caused by optical resonance (Born & Wolf, 1999; Kerker, 1989). The optical resonance in microcavity is a subject of big interest, related to fluorescence and lasing in microspheres (Fields, 2000).

A small transparent contaminant particle on the surface works as a lens in the near-field region. It leads to 3D thermal expansion of the substrate, which is strongly different from the 1D thermal expansion model. Meanwhile this 1D model was considered for the last ten years as a basic model of dry laser cleaning.

The strong enhancement (about few tens) of laser intensity can be obtained within the region with size < 100 nm on the substrate under the particle. Naturally, this effect is very important for optical lithography and many other applications (Lu, 2000 c; Mosbacher, 2001, Huang, 2002 a).

The substrate strongly influenced the distribution of laser intensity in the near field region due to secondary scattering of reflected radiation (see in

Fig. 1). The necessity to take this secondary scattering effect into account in laser cleaning has been declared many times (Donovan, 1988), nevertheless exact analytic solution of this problem is surprisingly rigorous (Bobbert & Vlieger, 1986 a). Nevertheless, a practical example of calculations with this solution for laser cleaning problem was done just recently (Luk'yanchuk, 2000).

Another way is direct numerical solution of the Maxwell equation by finite difference method (Wojcik, 1987; Mishenko, 2000). Although this method is universal, it can be applied to particles of different shapes, etc.; it needs powerful computers and is not flexible for the analysis of numerous experimental situations.

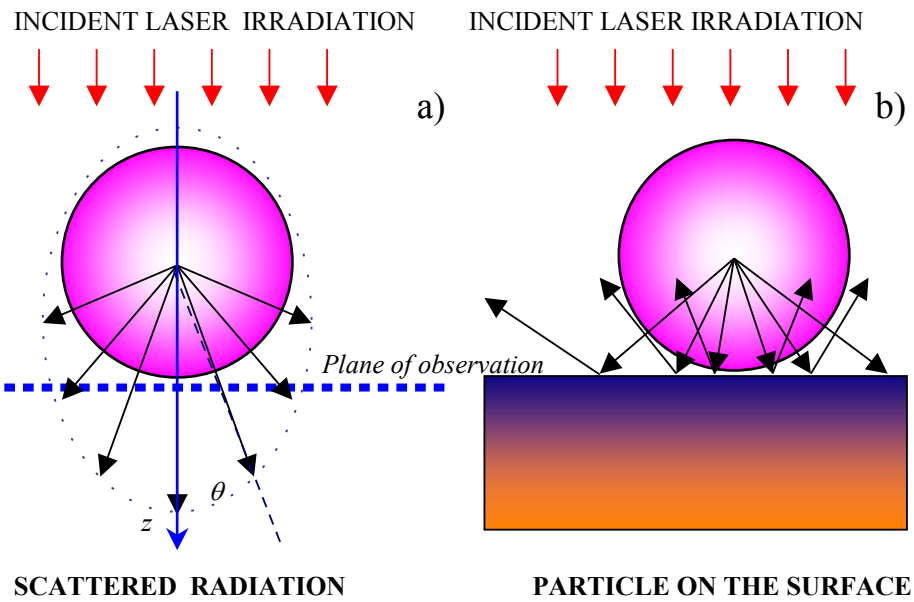

Fig. 1. Schematic for the particle scattering within the Mie theory, where the distribution of field is studied in arbitrary points, for example, in some observation plane (a). At typical consideration of the Mie theory (Born & Wolf, 1999) the incident plane wave propagates along the z-coordinate, and electric vector is directed along the x-coordinate. Particle on the surface (b) – the scattered radiation reflects from the surface and participates in the secondary scattering.

The methods of "intermediate power" like semianalytical field calculations using the Multiple Multipole (MMP) technique (Hafner, 1990) and ring multipoles (Zheng, 1990) should be mentioned. An example of calculations with these methods was done just recently (Münzer, 2002).

A careful calculation of intensity distribution permits to use more realistic "input" numbers for the further solution of the heat and thermal expansion problems. The goal of the given paper is to present the results of an examination of the mentioned optical problems and to discuss the basic influence of these effects on the efficiency of dry laser cleaning.

2. Optical resonance and near-field effects within the Mie theory

The initial step in laser cleaning is the absorption and scattering of laser light. In fact, many peculiarities of the scattering process can be understood on the basis of the Mie theory, where the particle is considered as a perfect sphere. This theory is discussed in detail in many books (Born & Wolf, 1999; Barber & Hill, 1990; Stratton, 1941; Kerker, 1969; Van de Hulst, 1981; Bohren & Huffman, 1983).

We consider that the amplitude of the electric vector of the incident plane wave is normalized to unity, and the wave propagates along the z-coordinate (positive direction), electric vector is directed along the *x*-coordinate, and magnetic vector along the *y*-coordinate. In the spherical coordinate system $\{r, \theta, \varphi\}$ with the origin, situated at the sphere center, this plane wave can be expressed as:

$$
\begin{aligned}
E_r &= e^{i k_m r\cos\theta} \sin\theta \cos\varphi, & H_r &= \sqrt{\varepsilon_m}\, e^{i k_m r\cos\theta} \sin\theta \sin\varphi, \\
E_\theta &= e^{i k_m r\cos\theta} \cos\theta \cos\varphi, & H_\theta &= \sqrt{\varepsilon_m}\, e^{i k_m r\cos\theta} \cos\theta \sin\varphi, \\
E_\varphi &= -e^{i k_m r\cos\theta} \sin\varphi, & H_\varphi &= \sqrt{\varepsilon_m}\, e^{i k_m r\cos\theta} \cos\varphi.
\end{aligned}
\qquad (1)
$$

Here ε_m is a complex dielectric permittivity of media, $\sqrt{\varepsilon_m} = n_m + i\kappa_m$. The wave vector of radiation in the media is indicated by $k_m = 2\pi\sqrt{\varepsilon_m}/\lambda$, where λ is the wavelength of radiation. In a similar way we shall indicate

the corresponding values for the particle as $\sqrt{\varepsilon_p} = n_p + i\kappa_p$ and $k_p = 2\pi\sqrt{\varepsilon_p}/\lambda$. The wave vector for vacuum is indicated by $k_0 = 2\pi/\lambda$.

In terms of the spherical waves the fields (1) are expressed as following (index "*i*" indicates the incident wave):

$$E_r^{(i)} = \frac{\cos\varphi}{(k_m r)^2} \sum_{\ell=1}^{\infty} i^{\ell-1} (2\ell+1)\, \psi_\ell(k_m r)\, P_\ell^{(1)}(\cos\theta),$$

$$E_\theta^{(i)} = -\frac{\cos\varphi}{k_m r} \sum_{\ell=1}^{\infty} i^{\ell-1} \frac{2\ell+1}{\ell(\ell+1)} \left[\psi'_\ell(k_m r)\, P_\ell^{(1)'}(\cos\theta) \sin\theta - i\,\psi_\ell(k_m r) \frac{P_\ell^{(1)}(\cos\theta)}{\sin\theta} \right],$$

$$E_\varphi^{(i)} = -\frac{\sin\varphi}{k_m r} \sum_{\ell=1}^{\infty} i^{\ell-1} \frac{2\ell+1}{\ell(\ell+1)} \left[\psi'_\ell(k_m r) \frac{P_\ell^{(1)}(\cos\theta)}{\sin\theta} - i\,\psi_\ell(k_m r)\, P_\ell^{(1)'}(\cos\theta) \sin\theta \right],$$

$$H_r^{(i)} = \frac{\sqrt{\varepsilon_m}\sin\varphi}{(k_m r)^2} \sum_{\ell=1}^{\infty} i^{\ell-1} (2\ell+1)\, \psi_\ell(k_m r)\, P_\ell^{(1)}(\cos\theta), \qquad (2)$$

$$H_\theta^{(i)} = i\frac{\sin\varphi}{k_0 r} \sum_{\ell=1}^{\infty} i^{\ell-1} \frac{2\ell+1}{\ell(\ell+1)} \left[\psi_\ell(k_m r) \frac{P_\ell^{(1)}(\cos\theta)}{\sin\theta} + i\,\psi'_\ell(k_m r)\, P_\ell^{(1)'}(\cos\theta) \sin\theta \right],$$

$$H_\varphi^{(i)} = -i\frac{\cos\varphi}{k_0 r} \sum_{\ell=1}^{\infty} i^{\ell-1} \frac{2\ell+1}{\ell(\ell+1)} \left[\psi_\ell(k_m r) P_\ell^{(1)'}(\cos\theta) \sin\theta + i\,\psi'_\ell(k_m r) \frac{P_\ell^{(1)}(\cos\theta)}{\sin\theta} \right],$$

where the radial dependence is expressed through the Bessel function (regular at $\rho = 0$) and prime indicates differentiation

$$\psi_\ell(\rho) = \sqrt{\frac{\pi\rho}{2}}\, J_{\ell+\frac{1}{2}}(\rho), \quad \psi'_\ell(\rho) = \frac{\partial\psi_\ell(\rho)}{\partial\rho}. \qquad (3)$$

The angular dependence in (2) is related to spherical functions, where $P_n^{(m)}(x)$ are associated Legendre polynomials. There is a well-known problem important for numerical calculations and related to the cutting of

sums in (2) by value $\ell \le \ell_{max}$ (Barber & Hill, 1990). The recommended values are given by $\ell_{\max} \approx q + 4q^{1/3} + 1$, where q is the corresponding size parameter. The scattered field for the non-magnetic particle (μ = 1) immersed in vacuum is presented by (index "*s* " stands for indication of the scattered wave):

$$E_r^{(s)} = \frac{\cos\varphi}{(k_m r)^2} \sum_{\ell=1}^{\infty} \ell(\ell+1)\, {}^{e}B_\ell\, \zeta_\ell(k_m r) P_\ell^{(1)}(\cos\theta),$$

$$E_\theta^{(s)} = -\frac{\cos\varphi}{k_m r} \sum_{\ell=1}^{\infty} \left[{}^{e}B_\ell\, \zeta_\ell'(k_m r) P_\ell^{(1)'}(\cos\theta) \sin\theta - i\ {}^{m}B_\ell\, \zeta_\ell(k_m r) \frac{P_\ell^{(1)}(\cos\theta)}{\sin\theta} \right],$$

$$E_\varphi^{(s)} = -\frac{\sin\varphi}{k_m r} \sum_{\ell=1}^{\infty} \left[{}^{e}B_\ell\, \zeta_\ell'(k_m r) \frac{P_\ell^{(1)}(\cos\theta)}{\sin\theta} - i\ {}^{m}B_\ell\, \zeta_\ell(k_m r) P_\ell^{(1)'}(\cos\theta) \sin\theta \right], \tag{4}$$

$$H_r^{(s)} = \frac{\sqrt{\varepsilon_m}\sin\varphi}{(k_m r)^2} \sum_{\ell=1}^{\infty} \ell(\ell+1)\ {}^{m}B_\ell\, \zeta_\ell(k_m r) P_\ell^{(1)}(\cos\theta),$$

$$H_\theta^{(s)} = i\frac{\sin\varphi}{k_0 r} \sum_{\ell=1}^{\infty} \left[{}^{e}B_\ell\, \zeta_\ell(k_m r) \frac{P_\ell^{(1)}(\cos\theta)}{\sin\theta} + i\ {}^{m}B_\ell\, \zeta_\ell'(k_m r) P_\ell^{(1)'}(\cos\theta) \sin\theta \right],$$

$$H_\varphi^{(s)} = -i\frac{\cos\varphi}{k_0 r} \sum_{\ell=1}^{\infty} \left[{}^{e}B_\ell\, \zeta_\ell(k_m r) P_\ell^{(1)'}(\cos\theta) \sin\theta + i\ {}^{m}B_\ell\, \zeta_\ell'(k_m r) \frac{P_\ell^{(1)}(\cos\theta)}{\sin\theta} \right],$$

where

$$\zeta_\ell(\rho) = \rho\, h_\ell^{(1)}(\rho), \qquad \zeta_\ell'(\rho) = \frac{\partial \zeta_\ell(\rho)}{\partial \rho}. \tag{5}$$

Here $h_\ell^{(1)}$ is related to the Hankel function, i.e. the Bessel function of the third kind, which vanished at infinity

$$h_\ell^{(1)}(\rho) = H^{(1)}_{\ell+\frac{1}{2}}(\rho) = J_{\ell+\frac{1}{2}}(\rho) + iN_{\ell+\frac{1}{2}}(\rho), \tag{6}$$

where $N_\ell(\rho)$ is the Neumann function (designation $Y_\ell(\rho)$ is used in some books for this function).

Coefficients ${}^eB_\ell$ and ${}^mB_\ell$ in formulae (4) are given by

$$ {}^eB_\ell = i^{\ell+1}\frac{2\ell+1}{\ell(\ell+1)}a_\ell, \qquad {}^mB_\ell = i^{\ell+1}\frac{2\ell+1}{\ell(\ell+1)}b_\ell, \tag{7} $$

where a_ℓ and b_ℓ are defined as

$$ \begin{aligned} a_\ell &= \frac{q_p\psi'_\ell(q_m)\psi_\ell(q_p)-q_m\psi_\ell(q_m)\psi'_\ell(q_p)}{q_p\varsigma'_\ell(q_m)\psi_\ell(q_p)-q_m\psi'_\ell(q_p)\varsigma_\ell(q_m)}\ , \ q_m = k_m a\ , \\ b_\ell &= \frac{q_p\psi'_\ell(q_p)\psi_\ell(q_m)-q_m\psi_\ell(q_p)\psi'_\ell(q_m)}{q_p\psi'_\ell(q_p)\varsigma_\ell(q_m)-q_m\psi_\ell(q_p)\varsigma'_\ell(q_m)}, \ \ q_p = k_p a\ . \end{aligned} \tag{8} $$

The internal fields (indicated by index "*a*") inside the particle are given by

$$ \begin{aligned} E_r^{(a)} &= \frac{\cos\varphi}{(k_p r)^2}\sum_{\ell=1}^{\infty}\ell(\ell+1)\ {}^eA_\ell\ \psi_\ell(k_p r)P_\ell^{(1)}(\cos\theta), \\ E_\theta^{(a)} &= -\frac{\cos\varphi}{k_p r}\sum_{\ell=1}^{\infty}\left[{}^eA_\ell\ \psi'_\ell(k_p r)P_\ell^{(1)'}(\cos\theta)\sin\theta - i\ {}^mA_\ell\ \psi_\ell(k_p r)\frac{P_\ell^{(1)}(\cos\theta)}{\sin\theta}\right], \\ E_\varphi^{(a)} &= -\frac{\sin\varphi}{k_p r}\sum_{\ell=1}^{\infty}\left[{}^eA_\ell\ \psi'_\ell(k_p r)\frac{P_\ell^{(1)}(\cos\theta)}{\sin\theta} - i\ {}^mA_\ell\ \psi_\ell(k_p r)P_\ell^{(1)'}(\cos\theta)\sin\theta\right], \\ H_r^{(a)} &= \frac{\sqrt{\varepsilon_p}\ \sin\varphi}{(k_p r)^2}\sum_{\ell=1}^{\infty}\ell(\ell+1)\ {}^mA_\ell\ \psi_\ell(k_p r)P_\ell^{(1)}(\cos\theta), \\ H_\theta^{(a)} &= i\frac{\sin\varphi}{k_0 r}\sum_{\ell=1}^{\infty}\left[{}^eA_\ell\ \psi_\ell(k_p r)\frac{P_\ell^{(1)}(\cos\theta)}{\sin\theta} + i\ {}^mA_\ell\ \psi'_\ell(k_p r)P_\ell^{(1)'}(\cos\theta)\sin\theta\right], \\ H_\varphi^{(a)} &= -i\frac{\cos\varphi}{k_0 r}\sum_{\ell=1}^{\infty}\left[{}^eA_\ell\ \psi_\ell(k_p r)P_\ell^{(1)'}(\cos\theta)\sin\theta + i\ {}^mA_\ell\ \psi'_\ell(k_p r)\frac{P_\ell^{(1)}(\cos\theta)}{\sin\theta}\right]. \end{aligned} \tag{9} $$

Coefficients ${}^{e}A_\ell$ and ${}^{m}A_\ell$ in formulae (9) are given by

$$ {}^{e}A_\ell = i^{\ell+1}\frac{2\ell+1}{\ell(\ell+1)}c_\ell\,, \qquad {}^{m}A_\ell = i^{\ell+1}\frac{2\ell+1}{\ell(\ell+1)}d_\ell\,, \tag{10} $$

where c_ℓ and d_ℓ are defined as

$$ \begin{aligned} c_\ell &= -\frac{q_p\left[\varsigma'_\ell(q_m)\psi_\ell(q_m)-\varsigma_\ell(q_m)\psi'_\ell(q_m)\right]}{q_p\varsigma'_\ell(q_m)\psi_\ell(q_p)-q_m\psi'_\ell(q_p)\varsigma_\ell(q_m)}\,, \\ d_\ell &= \frac{q_p\left[\varsigma'_\ell(q_m)\psi_\ell(q_m)-\varsigma_\ell(q_m)\psi'_\ell(q_m)\right]}{q_p\psi'_\ell(q_p)\varsigma_\ell(q_m)-q_m\psi_\ell(q_p)\varsigma'_\ell(q_m)}\,. \end{aligned} \tag{11} $$

The time-averaged Poynting vector gives the power per unit of area carried by the wave; see e.g. (Stratton, 1941):

$$ \mathbf{S} = \frac{1}{2}\,\mathrm{Re}\left\{\mathbf{E}\times\mathbf{H}^{\bullet}\right\}. \tag{12} $$

The z-component of this vector for the plane wave (1) is given by $S_z = \left\langle \cos^2\omega t\right\rangle = 1/2$. This value characterizing the homogeneous light intensity falls normally to $\{x, y\}$ plane. In some books (Barber & Hill, 1990) the light intensity is defined as

$$ I = \mathbf{E}\cdot\mathbf{E}^{*} \equiv \left|\mathbf{E}\right|^2. \tag{13} $$

Definitions $I = S_z$ and $I = \left|\mathbf{E}^2\right|$ yield the same *time-averaged* value for a purely transversal electromagnetic wave, e.g. for the plane wave (1). For the near-field region (with the longitudinal field components) these two intensities are different.

As it was mentioned a small transparent particle can work as a focusing lens even at the particle size, $2a$, comparable with radiation wavelength, λ. The enhanced laser intensity arises near the particle surface at the distances, which are small compared to λ (near-field effects). This behavior can be clearly seen from Fig. 2, where the intensity distributions are shown in $\{x, z\}$ and $\{y, z\}$ planes.

For practical applications it is important to understand how these distributions vary with radiation wavelengths. As an example Fig. 3 shows the distribution of laser intensity along the z - axis of the particle with radius a = 0.5 μm for radiation with λ = 1064, 532, 266 and 157 nm. The z - axis coincides with the direction of the wave vector for incident radiation. Particle is nonabsorbing (κ = 0) with refractive index n = 1.6. The background media is vacuum. Intensity is understood as a square of the electric vector. One can see from the Fig. 3 that both maximal intensities (inside and outside the particle) increase with a decrease of the radiation wavelength. Oscillations inside the particle (standing wave pattern) are resulting from interference between the refracted and internally reflected field components, while outside the particle they are caused by interference of incident and scattered radiation (Barber & Hill, 1990).

The maximal intensity out of the particle (see in Fig. 3 a) can be by the order of magnitude higher than the incident intensity. With $a \approx (2-3)\lambda$ this intensity may exceed the incident intensity by two orders of magnitude (see in Fig. 3 c, d). This maximal intensity is situated exactly on the surface (Fig. 3a, b, c) or below the particle (Fig. 3 d).

The distribution of laser intensity within the tangential $\{x, y\}$ - plane under the particle is shown in Fig. 4. One can see the high localization of laser intensity. It is clear that this effect can be used for optical lithography and nanopatterning of the surface (Lu, 2000c, 2002; Mosbacher, 2001; Huang, 2002 a, b) as well as for near-field microscopy (Münzer, 2001).

The extinction, absorption and scattering cross sections are given by $\sigma_{ext} = \pi a^2 Q_{ext}$, $\sigma_{abs} = \pi a^2 Q_{abs}$, $\sigma_{sca} = \pi a^2 Q_{sca}$, where related efficiencies Q for polarized and non-polarized light are presented by (Born & Wolf, 1999):

$$Q_{ext} = \frac{2}{q^2}\sum_{\ell=1}^{\infty}(2\ell+1)Re(a_\ell + b_\ell), \quad Q_{sca} = \frac{2}{q^2}\sum_{\ell=1}^{\infty}(2\ell+1)\left\{|a_\ell|^2 + |b_\ell|^2\right\}, \qquad (14)$$

$$\overline{cos\,\theta}\cdot Q_{sca} = \frac{4}{q^2}\sum_{\ell=1}^{\infty}\frac{\ell(\ell+2)}{\ell+1}Re\left(a_\ell a_{\ell+1}^* + b_\ell b_{\ell+1}^*\right) + \frac{4}{q^2}\sum_{\ell=1}^{\infty}\frac{2\ell+1}{\ell(\ell+1)}Re\left(a_\ell b_\ell^*\right),$$

$$Q_{abs} = Q_{ext} - Q_{sca}, \quad Q_{pr} = Q_{ext} - \overline{\cos\theta}\cdot Q_{sca},$$

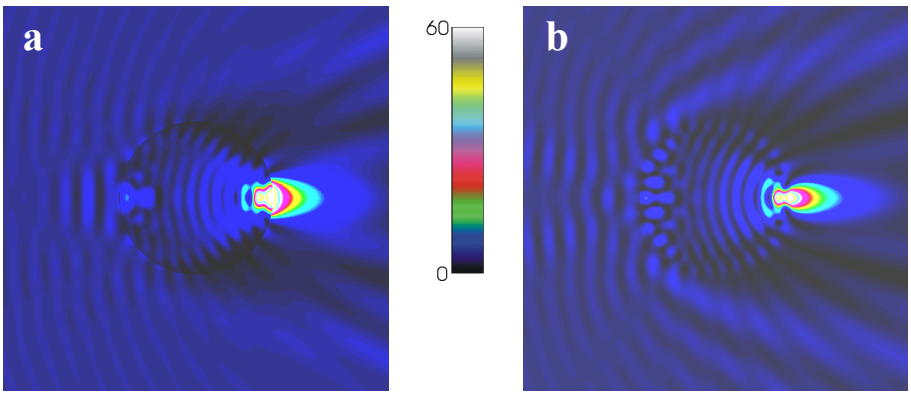

Fig. 2. Intensity distribution, $I = |E|^2$, inside and outside the 1 μm SiO_2 particle, illuminated by radiation with λ = 266 nm, and polarization parallel (a) and perpendicular (b) to image plane. The maximum intensity enhancement in calculations is about 60 for both regions.

where the star indicates a complex conjugation, and size parameter is given by $q = k_0 a = 2\pi a/\lambda$. Q_{pr} describes the effects of radiation pressure (van de Hulst, 1981).

The extinction versus size parameter, q, demonstrates the "low frequency" transition oscillations, and "high frequency" modulation, which can be seen in Fig. 5, where the dependence $Q_{ext}(q)$ is shown for sphere with n = 1.6. At a very big size parameter $q \to \infty$ extinction tends to value $Q_{ext} = 2$; this is the so-called "extinction paradox". The oscillations are related to excitation of partial **E** and **H** resonance modes (Born & Wolf, 1999). The extinction is the integral characteristic caused by far-field scattering. This scattering diagram in x-y plane is given by modes (Born & Wolf, 1999):

$$I_{||}^{(far)} = \left(\frac{\lambda}{2\pi r}\right)^2 \left| \sum_{\ell=1}^{\infty} (-i)^{\ell} \left[{}^{e}B_{\ell} P_{\ell}^{(1)'}(\cos\theta)\sin\theta - {}^{m}B_{\ell} \frac{P_{\ell}^{(1)}(\cos\theta)}{\sin\theta} \right] \right|^2, \qquad (15)$$

$$I_{\perp}^{(far)} = \left(\frac{\lambda}{2\pi r}\right)^2 \left| \sum_{\ell=1}^{\infty} (-i)^{\ell} \left[{}^{e}B_{\ell} \frac{P_{\ell}^{(1)}(\cos\theta)}{\sin\theta} - {}^{m}B_{\ell} P_{\ell}^{(1)'}(\cos\theta)\sin\theta \right] \right|^2.$$

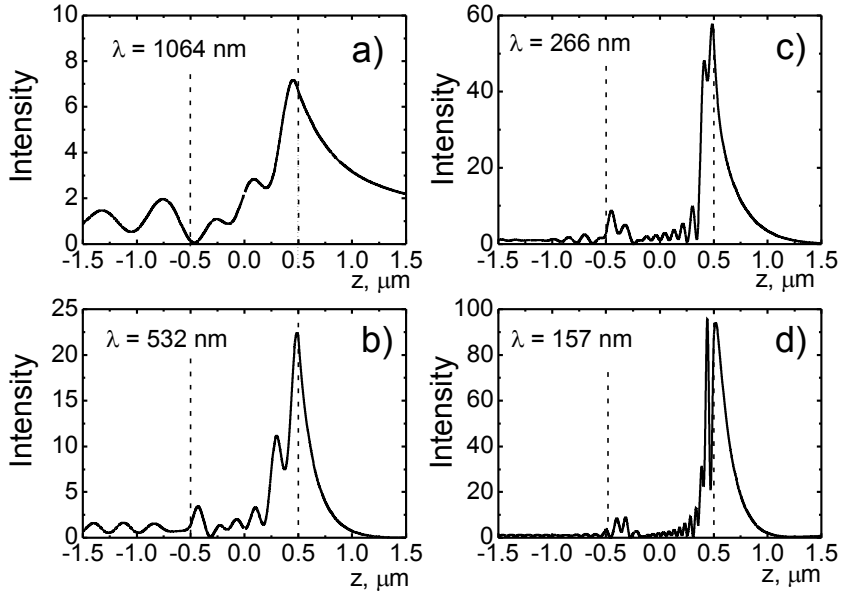

Fig. 3. Distribution of laser intensity $I = \left|\mathbf{E}^2\right|$ inside and outside the particle with radius a = 0.5 μm for different radiation wavelength λ. Particle is considered to be nonabsorbing ($\kappa = 0$) with refractive index n = 1.6. Background media is vacuum. Intensity is understood as a square of the electric vector.

Formulae (15) follow from the asymptotic expansion of the electric field in the far-field region $r \gg \lambda$ (we use indexes $^{(far)}$ and $^{(nf)}$ for indication far field and near field distributions). Within the near field region, where $r \sim \lambda$, instead of (15) one should write the exact formulae for the field components:

$$I_{\parallel}^{(nf)} = \left(\frac{\lambda}{2\pi r}\right)^2 \left| \sum_{\ell=1}^{\infty} (-i)^{\ell} \left[{}^{e}B_{\ell}\zeta_{\ell}'(kr) P_{\ell}^{(1)\prime}(\cos\theta)\sin\theta \; - i\, {}^{m}B_{\ell}\zeta_{\ell}(kr) \frac{P_{\ell}^{(1)}(\cos\theta)}{\sin\theta} \right] \right|^2$$

(16)

$$I_{\perp}^{(nf)} = \left(\frac{\lambda}{2\pi r}\right)^2 \left| \sum_{\ell=1}^{\infty} (-i)^{\ell} \left[{}^{e}B_{\ell}\zeta_{\ell}'(kr) \frac{P_{\ell}^{(1)}(\cos\theta)}{\sin\theta} \; - i\, {}^{m}B_{\ell}\zeta_{\ell}(kr) P_{\ell}^{(1)\prime}(\cos\theta)\sin\theta \right] \right|^2$$

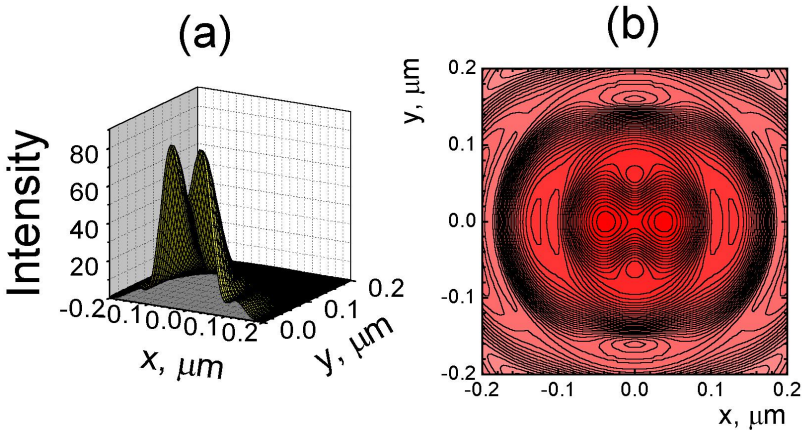

Fig. 4. Distribution of laser intensity within the tangential plane under the particle with radius a = 0.5 μm. (a) 3D picture of the intensity distribution. (b) Topography of the intensity distribution in $\{x, y\}$ - plane. Particle is considered to be nonabsorbing (κ = 0) with refractive index n = 1.5. Size parameter: $q = 2\pi a/\lambda = 20$, i.e. $\lambda \approx 157$ nm. Intensity is understood as a square of the electric vector.

These diagrams are shown in Fig. 6. One can see a big difference in the far field and near field intensity distributions, e.g. the main directional lobe in the near field region is narrower in the far-field region, new lobes appear in back scattering diagram, etc.

According to this diagram one would expect that optical resonance strongly influenced the near-field scattering characteristics compared to far-field characteristics. As an example, in Fig. 7 the laser radiation intensity under the transparent particle is shown. The calculation is performed on the basis of the Mie theory. This intensity is clearly a near-field characteristic. One can see variations of this intensity are by the order of magnitude higher than in the extinction (far-field characteristic) shown in Fig. 5. Big variations of intensity inside the particle (see in Fig. 3) are important for nonlinear optics in microspheres (Fields, 2000).

The concept of the optical resonance suggests high variations in cleaning efficiency with a small change in size parameter. It is different from conventional point of view (Lu, 2000 a; Mosbacher, 2001), which suggests the dry laser cleaning efficiency varies monotonously with particle size. A similar comment can be done with respect to increase of cleaning

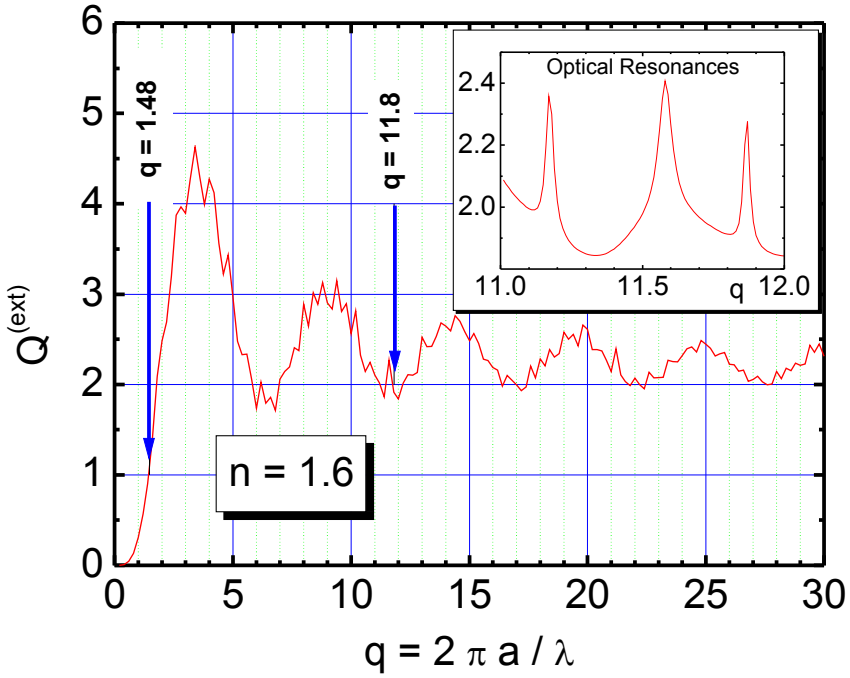

Fig. 5. The extinction coefficient $Q^{(ext)}$ versus size parameter q is calculated with the help of (14) for a spherical silica particle with $n = 1.6$. The arrows indicate particular values, examined in the paper of Lu, 2000 a: $q = 1.48$ ($a = 0.25$ μm, $\lambda = 1.064$ μm) and $q = 11.81$ ($a = 0.5$ μm, $\lambda = 0.266$ μm). The insertion shows the resonance structure within the range $11 \le q \le 12$.

efficiency for shorter wavelength radiation (Lu, 2000). Fig. 8 shows a big effect in the intensity distribution within the range of size parameter variation between the two nearest optical resonances (maximal intensity varies twice, when the q varies just of 2 % !). Once again, we should remind that under the approximation of the Mie theory one ignores the secondary scattering effects, produced by radiation reflected from the substrate surface, see in Fig. 1.

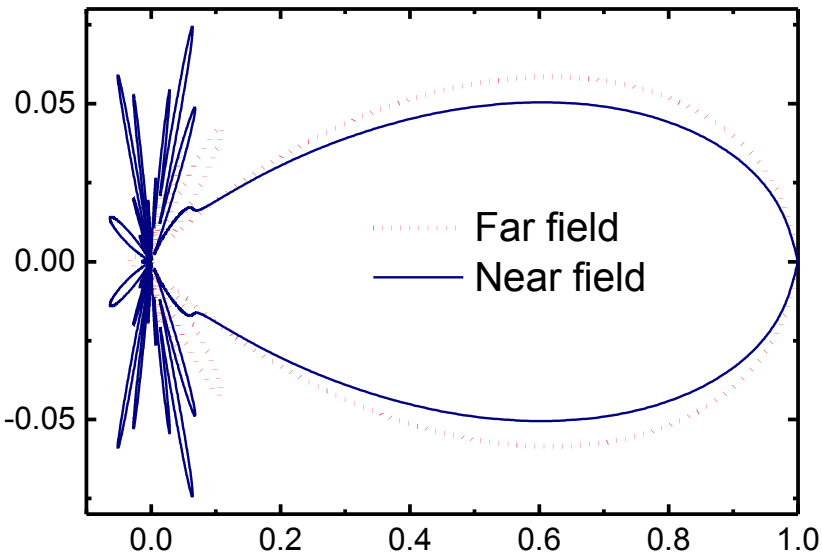

Fig. 6. The polar diagrams for the far field ($r \gg \lambda$) and near field ($r = a \sim \lambda$, $a = 0.5$ μm, $\lambda = 0.266$ μm) scattering. The standard representation (Born & Wolf, 1999) is used, i.e. the polar angle corresponds to θ, while the radius vector in the plots is proportional to the perpendicular intensity $I_\perp$. The diagrams are normalized to unity in the direction of direct scattering, i.e. at $\theta = 0$.

3. Particle on the surface. Beyond the Mie theory.

The effect of secondary scattering can be qualitatively understood under the following simplification. Let us consider that reflected radiation is presented by a plane wave (in reality it is a spherical wave). This yields:

$$I = \frac{I_m(0)}{1 - R_0 I_m(\pi)}, \tag{17}$$

where R_0 is reflection coefficient, and $I_m(\theta)$ is a distribution of intensity versus polar angle from the Mie theory.

Although formula (17) is applicable just for $R_0 I_m(\pi) < 1$ and exceeds the true value of intensity, it shows by a correct way the main effect of reflection, i.e. a fast increase of field enhancement at resonant points with increase of size parameter.

One can see in Fig. 7 important consequences of the substrate reflection onto the optical resonance effect. Oscillations of the intensity versus size parameter become more pronounced with a higher surface reflection coefficient. The effect can be seen even with a small reflection R_0 = 0.02. The surface played the role of a resonator mirror for a spherical cavity. This, in turn, leads to a sharpening in intensity distribution. Inhomogeneity in laser intensity leads to temperature distribution inhomogeneity, producing a "hot point" under the particle. It results in 3D-thermoelastic deformations, which are quite different from conventional 1D thermal expansion model (Kelly, 1993; Lu, 1997). The important limitation of 1D model is that it does not permit a fast backward motion of the substrate surface. As a result, 1D model predicts threshold fluences for laser cleaning, which exceed the experimental values by the order of magnitude (Luk'yanchuk, 2001, 2002c; Zheng, 2001; Arnold, 2002).

Formula (17) is quite crude and valid just for qualitative consideration. For quantitative analysis one can use the exact solution of the problem "particle on the surface". Bobbert & Vliger, 1986 a, found this solution. Although this solution is rigorous, the idea of the solution is rather simple.

Let a wave $\mathbf{V}^{in}$ (e.g. a plane wave) be incident on this system. If the sphere was absent we could satisfy the boundary conditions at the interface between the ambient and the substrate by adding a wave $\mathbf{V}^{R}$ (just Fresnel reflection in the case of a plane wave). In the presence of the sphere there will be an additional scattered wave $\mathbf{W}^{S}$ as a result of the currents flowing inside the sphere. But this wave will also be reflected by the substrate – i.e. induce currents flowing inside the substrate and will give rise to a secondary reflected scattered wave $\mathbf{V}^{SR}$. The fields $\mathbf{V}^{SR}$ and $\mathbf{W}^{S}$, once again, should be linearly related by some matrix $\hat{\mathbf{A}}$, characterizing the reflection of spherical waves by the substrate:

$$\mathbf{V}^{SR} = \hat{\mathbf{A}} \cdot \mathbf{W}^{S} . \qquad (18)$$

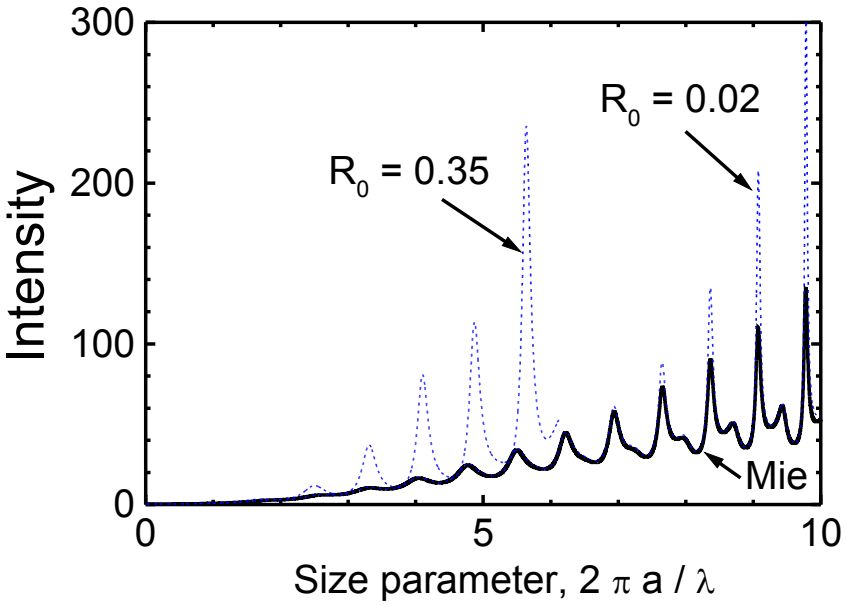

Fig. 7. The intensity distribution under the particle with refractive index n = 1.6. Solid line presents solution from the Mie theory. Dashed lines show variation in intensity, caused by reflection of substrate. These lines are according to approximating formula (17) for small (R_0 = 0.02) and high (R_0 = 0.35) substrate reflection coefficients.

Consider (18) together with overall equation

$$\mathbf{W}^S = \hat{\mathbf{B}} \cdot \left(\mathbf{V}^{in} + \mathbf{V}^R + \mathbf{V}^{SR} \right). \qquad (19)$$

one can easily find the formal solution in terms of $\mathbf{V}^{in}$ and $\mathbf{V}^{\mathrm{R}}$ vectors:

$$\mathbf{W}^{\mathrm{S}} = (\hat{1} - \hat{\mathbf{B}}\hat{\mathbf{A}})^{-1} \cdot \hat{\mathbf{B}} \cdot (\mathbf{V}^{\mathrm{in}} + \mathbf{V}^{\mathrm{R}}) . \qquad (20)$$

Thus, the technical problem is related to the calculation of "reflection matrix", $\hat{\mathbf{A}}$, and the inverse matrix $\left(\hat{\mathbf{1}} - \hat{\mathbf{B}}\hat{\mathbf{A}}\right)^{-1}$ in the above equation. The

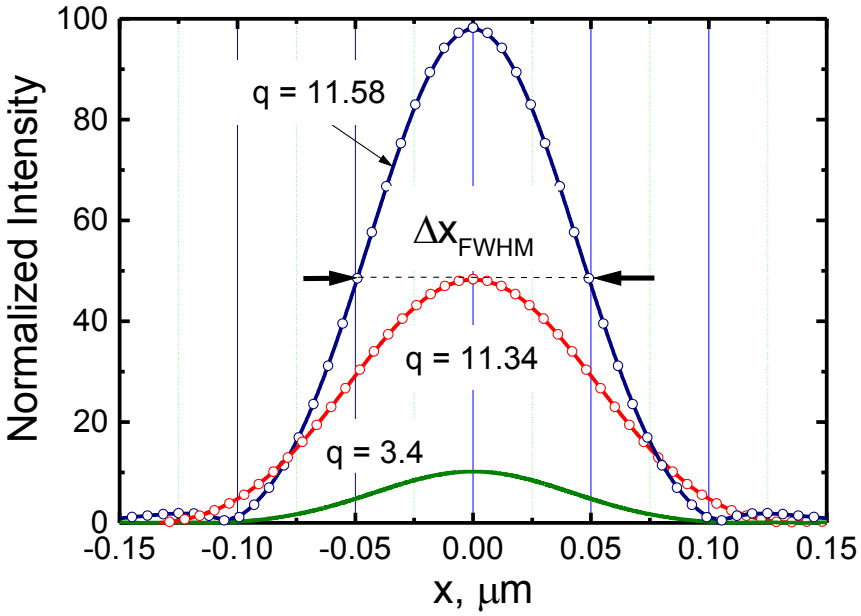

Fig. 8. The intensity distributions (z-component of the Poynting vector) along the *x*-coordinate for different size parameters q. Values $q = 11.58$ and $q = 11.34$ correspond to the nearest maximal and minimal values of $Q^{(ext)}$ within particular optical resonance (see insertion in Fig. 5). We use in calculations $\lambda = 0.266$ μm and the variation of the size parameter was due to a variation in the particle size. For two upper curves particle sizes were, $2a = 0.98$ and 0.96 μm, respectively.

numerical calculations with exact formula (20) were presented by (Luk'yanchuk, 2000) for the SiO_2 particles on the silicon substrate. In papers of (Bobbert, 1986 a, b) authors used the expansion of inverse matrix. Some particular cases were also analyzed: perfectly conducting substrate or far-away scattered field. Examples of practical calculations for Si particles on the silicon substrate were presented by Wojcik, 1987. They were done with the help of discrete numerical solutions of Maxwell's equations. This direct way needs a powerful computer or even supercomputer (calculations were performed with CRAY 2 supercomputer). Although during the last

decade there was big progress with these computations (Mishenko, 2000), the exact solutions are still interesting for both, practical calculations, and as a test problem for solution of Maxwell equations. The semianalytical field calculations using the Multiple Multipole (MMP) technique (Hafner, 1990) and ring multipoles (Zheng, 1990) were mentioned above. An example of calculations with these methods was demonstrated recently for polystyrene particles on the Si substrate (Münzer, 2002).

The $\hat{\mathbf{B}}$-matrix in (20) is presented by Mie formulae, while for the $\hat{\mathbf{A}}$-matrix (which describes reflection of the spherical wave) the following formulae were found by Bobbert & Vlieger, 1986 a:

$$A_{\ell',m';\,\ell,m} = i^{\ell'-1}\sqrt{\frac{2\ell'+1}{\ell'(\ell'+1)}}\,(-1)^{m-1}\delta_{mm'}\int_0^{\pi/2-i\infty} d\alpha\ \sin\alpha\ e^{2iq\cos\alpha}\,a^{m}_{\ell',f';\,\ell,f}\ , \quad (21)$$

with the abbreviations

$$a^{m}_{\ell',e;\,\ell,e} = r_p(\cos\alpha)\,\widetilde{V}^{m}_{\ell}(\cos\alpha)\,d^{\ell'}_{m,-}(\pi-\alpha) + r_s(\cos\alpha)\,\widetilde{U}^{m}_{\ell}(\cos\alpha)\,d^{\ell'}_{m,+}(\pi-\alpha),$$

$$a^{m}_{\ell',h;\,\ell,e} = -i\,\{r_p(\cos\alpha)\,\widetilde{V}^{m}_{\ell}(\cos\alpha)\,d^{\ell'}_{m,+}(\pi-\alpha) + r_s(\cos\alpha)\,\widetilde{U}^{m}_{\ell}(\cos\alpha)\,d^{\ell'}_{m,-}(\pi-\alpha)\},$$

$$a^{m}_{\ell',e;\,\ell,h} = i\,\{r_p(\cos\alpha)\,\widetilde{U}^{m}_{\ell}(\cos\alpha)\,d^{\ell'}_{m,-}(\pi-\alpha) + r_s(\cos\alpha)\,\widetilde{V}^{m}_{\ell}(\cos\alpha)\,d^{\ell'}_{m,+}(\pi-\alpha)\},$$

$$a^{m}_{\ell',h;\,\ell,h} = r_p(\cos\alpha)\,\widetilde{U}^{m}_{\ell}(\cos\alpha)\,d^{\ell'}_{m,+}(\pi-\alpha) + r_s(\cos\alpha)\,\widetilde{V}^{m}_{\ell}(\cos\alpha)\,d^{\ell'}_{m,-}(\pi-\alpha),$$

(22)

$$\widetilde{U}^{m}_{\ell} = i^{1-\ell}\,\frac{\ell-1}{2}\left\{\sqrt{\frac{(\ell+m-1)(\ell+m)}{(2\ell-1)(2\ell+1)}}\,\widetilde{P}^{m-1}_{\ell-1} - \sqrt{\frac{(\ell-m-1)(\ell-m)}{(2\ell+1)(2\ell-1)}}\,\widetilde{P}^{m+1}_{\ell+1}\right\}$$

$$-i^{-1-\ell}\,\frac{\ell+2}{2}\left\{\sqrt{\frac{(\ell-m+1)(\ell+m+2)}{(2\ell+3)(2\ell+1)}}\widetilde{P}^{m-1}_{\ell-1} + \sqrt{\frac{(\ell-m+1)(\ell+m+2)}{(2\ell+3)(2\ell+1)}}\widetilde{P}^{m+1}_{\ell+1}\right\},$$

(23)

$$\widetilde{V}_\ell^{\,m} = \frac{1}{2} i^{1-\ell} \left\{ \sqrt{(\ell - m + 1)(\ell + m)}\ \widetilde{P}_\ell^{\,m-1} - \sqrt{(\ell + m + 1)(\ell - m)}\ \widetilde{P}_\ell^{\,m+1} \right\},$$

where tilda indicates the normalized Legendre functions $\widetilde{P}_\ell^{\,m}(\cos\alpha) = \sqrt{(2\ell+1)\frac{(\ell-m)!}{(\ell+m)!}}\ P_\ell^m(\cos\alpha)$.

The function $d^{\ell}_{m,m'}(\alpha)$ is defined as:

$$d^{\ell}_{m,m'}(\alpha) \equiv \sqrt{(\ell+m')!(\ell-m')!(\ell+m)!(\ell-m)!} \sum_k (-1)^k \frac{(\cos\frac{\alpha}{2})^{2\ell+m'-m-2k} (\sin\frac{\alpha}{2})^{m-m'+2k}}{(\ell-m-k)!(\ell+m'-k)!(k+m-m')!k!} \tag{24}$$

and indexes plus and minus indicate the symmetrical and antisymmetrical combinations

$$\begin{aligned} d^{\ell'}_{m,-}(\pi-\alpha) &= \frac{1}{2}\left\{ d^{\ell'}_{m,1}(\pi-\alpha) - d^{\ell'}_{m,-1}(\pi-\alpha) \right\}, \\ d^{\ell'}_{m,+}(\pi-\alpha) &= \frac{1}{2}\left\{ d^{\ell'}_{m,1}(\pi-\alpha) + d^{\ell'}_{m,-1}(\pi-\alpha) \right\}. \end{aligned} \tag{25}$$

The $r_p(\cos\alpha)$ and $r_s(\cos\alpha)$ functions in (22) present the Fresnel reflection coefficients for parallel and perpendicular polarization. Coefficients *d* arise due to rotation matrix, for each plane wave propagating in another direction than the *z*-direction we need to express the basic Mie solution in rotated coordinate system (r,θ',φ') in terms of those in the coordinate system (r,θ,φ), i.e. transform the spherical harmonics. This transform can be done with the help of addition theorem for Legender polynomials, which yields (Rose, 1957):

$$\begin{aligned} Y_\ell^{m'}(\theta',\varphi') &= \sum_{m=-\ell}^{\ell} (-1)^{m-m'} D^{\ell}_{m,m'}(\beta,\alpha,\gamma)\, Y_\ell^{m}(\theta,\varphi), \\ D^{\ell}_{m,m'}(\beta,\alpha,\gamma) &= e^{-im\beta}\ d^{\ell}_{m,m'}(\alpha)\ e^{-im'\gamma}. \end{aligned} \tag{26}$$

Here rotation matrix D is expressed through the Euler angles (α, β, γ) arising during rotation of (r, θ, φ) system to obtain the (r, θ', φ') system. The argument $\pi - \alpha$ in formulae (22) and (25) expresses the angle of reflected light. Indexes f and f' in (21) indicate transitions between the electrical, $f = e$, and magnetic, $f = h$, components.

Suppose the incident wave vector $\mathbf{k}$ to be in the *x*-*z* plane of the coordinate system $\mathbf{k} = k\,(\sin\theta_i,\ 0,\ \cos\theta_i)$, k is the absolute value of the wave-vector, θ_i is the incident angle, and amplitude |**E**|=1. If the plane wave is *p*-polarized (electric vector in the plane of incidence i.e. *x*-*z* plane), $\mathbf{V}^{in}$ and $\mathbf{V}^{\mathrm{R}}$ have components, see in Bobbert & Vlieger, 1986 a:

$$
\begin{aligned}
{}^{e}v_{\ell}^{m\ \mathrm{in}} &= \frac{i^{\ell-1}}{k}\sqrt{\frac{2\ell+1}{\ell(\ell+1)}}\,(-1)^{m-1}\,d^{\ell}_{m,-}(\theta_i),\\
{}^{h}v_{\ell}^{m\ \mathrm{in}} &= -\frac{i^{\ell}}{k}\sqrt{\frac{2\ell+1}{\ell(\ell+1)}}\,(-1)^{m-1}\,d^{\ell}_{m,+}(\theta_i)\\
{}^{e}v_{\ell}^{m\ \mathrm{R}} &= \frac{i^{\ell-1}}{k}e^{2iq\cos\theta_i}\ r_p\,(\cos\theta_i)\ \sqrt{\frac{2\ell+1}{\ell(\ell+1)}}\,(-1)^{\ell}\,d^{\ell}_{m,-}(\theta_i),\\
{}^{h}v_{\ell}^{m\ \mathrm{R}} &= -\frac{i^{\ell}}{k}e^{2iq\cos\theta_i}\,r_p\,(\cos\theta_i)\sqrt{\frac{2\ell+1}{\ell(\ell+1)}}\,(-1)^{\ell-1}\,d^{\ell}_{m,+}(\theta_i).
\end{aligned}
\tag{27}
$$

If it is *s*-polarized (electric vector normal to the plane of incidence) $\mathbf{V}^{\mathrm{in}}$ and $\mathbf{V}^{\mathrm{R}}$ have following components:

$$
\begin{aligned}
{}^{e}v_{\ell}^{m\ \mathrm{in}} &= -\frac{i^{\ell}}{k}\sqrt{\frac{2\ell+1}{\ell(\ell+1)}}\,(-1)^{m-1}\,d^{\ell}_{m,+}(\theta_i),\\
{}^{h}v_{\ell}^{m\ \mathrm{in}} &= \frac{i^{\ell+1}}{k}\sqrt{\frac{2\ell+1}{\ell(\ell+1)}}\,(-1)^{m-1}\,d^{\ell}_{m,-}(\theta_i),\\
{}^{e}v_{\ell}^{m\ \mathrm{R}} &= -\frac{i^{\ell}}{k}\,e^{2iq\cos\theta_i}\ r_s(\cos\theta_i)\sqrt{\frac{2\ell+1}{\ell(\ell+1)}}(-1)^{\ell-1}d^{\ell}_{m,+}(\theta_i),\\
{}^{h}v_{\ell}^{m\ \mathrm{R}} &= \frac{i^{\ell+1}}{k}\,e^{2iq\cos\theta_i}\ r_s(\cos\theta_i)\ \sqrt{\frac{2\ell+1}{\ell(\ell+1)}}\,(-1)^{\ell}\,d^{\ell}_{m,-}(\theta_i).
\end{aligned}
\tag{28}
$$

With the incident, reflected and scattered waves available, the Debye potential with respect to the *total* electromagnetic field (which is necessary for calculation of Poynting vector), can be expressed as:

$$
\begin{aligned}
{}^{e}D(r) &= \sum_{\ell=1}^{\infty} \sum_{m=-\ell}^{\ell} \left\{ ({}^{e}v_{\ell}^{m\,\mathrm{in}} + {}^{e}v_{\ell}^{m\,\mathrm{R}} + {}^{e}v_{\ell}^{m\,\mathrm{SR}}) \Psi_{\ell}^{m}(r) + {}^{e}w_{\ell}^{m\,\mathrm{S}}\ \Pi_{\ell}^{m}(r) \right\}, \\
{}^{h}D(r) &= \sum_{\ell=1}^{\infty} \sum_{m=-\ell}^{\ell} \left\{ ({}^{h}v_{\ell}^{m\,\mathrm{in}} + {}^{h}v_{\ell}^{m\,\mathrm{R}} + {}^{h}v_{\ell}^{m\,\mathrm{SR}})\ \Psi_{\ell}^{m}(r) + {}^{h}w_{\ell}^{m\,\mathrm{S}}\ \Pi_{\ell}^{m}(r) \right\},
\end{aligned}
\tag{29}
$$

where ${}^{e}v_{\ell}^{m\,\mathrm{SR}}$ and ${}^{h}v_{\ell}^{m\,\mathrm{SR}}$ mean the corresponding elements of the vector $\mathbf{V}^{\mathrm{SR}}$, as given by (18), and scattering coefficients ${}^{e}w_{\ell}^{m\,\mathrm{S}}$ and ${}^{h}w_{\ell}^{m\,\mathrm{S}}$ are derived from (20). Functions Π_{l}^{m} and ψ_{l}^{m} are solutions of scalar Helmholtz equation:

$$
\Pi_{\ell}^{m} = h_{\ell}^{(1)}(kr)\, Y_{\ell}^{m}(\theta,\phi)\,, \quad \Psi_{\ell}^{m} = j_{\ell}(kr)\, Y_{\ell}^{m}(\theta,\phi)\,, \tag{30}
$$

where the spherical harmonics are defined by

$$
Y_{\ell}^{m}(\theta,\phi) = [(2\ell+1)\frac{(\ell-m)!}{(\ell+m)!}]^{1/2}\ P_{\ell}^{m}(\cos\theta)\, e^{\,im\phi}\,. \tag{31}
$$

Spherical Hankel and Bessel functions in (30) are given by formulae (6) and (3):

$$
h_{\ell}^{(1)}(\rho) \equiv \sqrt{\frac{\pi}{2\rho}}\ H_{\ell+1/2}^{(1)}(\rho)\,, \qquad j_{\ell}(\rho) \equiv \sqrt{\frac{\pi}{2\rho}}\ J_{\ell+1/2}(\rho)\,. \tag{32}
$$

The electric and magnetic fields can be derived from the Debye potentials (29) by a well-known formulae, see e.g. Born & Wolf, 1999:

$$
\mathbf{E} = \nabla\times\nabla\times\left(\mathbf{r}\ {}^{e}D\right) + ik\ \nabla\times(\mathbf{r}\ {}^{h}D)\,,
$$

$$\mathbf{H} = \sqrt{\varepsilon_m}\left[\nabla\times\nabla\times\left(\mathbf{r}\ {}^{h}D\right) - ik\nabla\times(\mathbf{r}\ {}^{e}D)\right]. \qquad (33)$$

Thus, formula (29) presents the final result of calculations, all quantaties within these formulae were defined above. Probably some of the written formulae were not explicitly derived in Bobbert 1986 a, b papers, but they follow from these papers after some simple transformations.

We use "Mathematica-4" software (Wolfram, 1999) for calculations. First of all we examine the calculation accuracy and different particular cases, some remarks should be done. First, the integrand in equation (21) contains a highly oscillating function. This is the so-called Weyl type integrals (Stratton, 1941; Morse & Feshbach, 1953; Bobbert & Vlieger, 1986 a) defined by

$$\Pi_{\ell}^{m}(r) = \frac{i^{-\ell}}{2\pi}\int_{0}^{2\pi} d\beta \int_{0}^{\pi/2-i\infty} \sin\alpha\, e^{ikr\cos\gamma}\, Y_{\ell}^{m}(\alpha,\beta)\, d\alpha\,, \qquad (34)$$

where $Y_{\ell}^{m}(\alpha,\beta)$ are the spherical harmonics, related to associated Legendre polynomials (Wolfram, 1999).

For typical calculations it was insufficient to use the Laguerre polynomial approximation method, which was recommended in Bobbert, 1986 b. Thus, everywhere we use the "honest" integration in (34). The integral (34) is defined in the plane of complex variable, α, along some special path. We construct the integration contour as

$$\alpha = \frac{\pi}{2}\frac{cx}{1+cx} + i\,cx\,, \qquad (35)$$

where c is any positive real value, and x varies from zero to infinity. Along this integration contour we found that, at the cost of longer calculation time, a stable value can be achieved. The matrix elements of $\hat{\mathbf{A}}$ have to be calculated only for non-negative m values, the negative parts can be mirrored as:

$$a_{l',e;l,e}^{-m} = a_{l',e;l,e}^{m},\quad a_{l',h;l,e}^{-m} = -a_{l',h;l,e}^{m},\quad a_{l',e;l,h}^{-m} = -a_{l',e;l,h}^{m},\quad a_{l',h;l,h}^{-m} = a_{l',h;l,h}^{m}\,. \qquad (36)$$

We found that the cut-off parameter $\ell_{\max}$ within the sum (29) should be *two units greater* than that recommended by Barber & Hill, 1990, i.e. $\ell_{\max} \approx q + 4q^{1/3} + 3$. We calculate not the field directly, but the Debye potentials, which should be further differentiated according to (33). This implies that higher accuracy can be achieved with this truncating level. Verification was made by setting the same refractive indexes for the substrate and the medium (the reflecting matrix is zero). The result was compared with the Mie scattering. Another verification was done by setting the reflex index of the particle equal to the medium (the scattering matrix is zero), the result was compared with the Fresnel reflection. The numerical deviation within all the calculated quantaties (**E**, **H**, Pointing vector) was less than 5% withing the range $r \le a$.

The results of calculations are presented in Figs. 9-11. These pictures illustrate the main peculiarities of "particle on the surface" solution compared with the conventional Mie theory.

From Fig. 9 one can see that the true solution demonstrates 1.5 times higher intensity in the center than the Mie solution. Here we set solution slightly below the substrate to see the absorbed radiation. This result was expected, because the multi-reflection of radiation between the particle and the substrate results in more energy flowing into the substate.

The FWHM for the intensity distribution is even smaller than for the Mie solution. It means that the near-field sharpening effect shown in Fig. 8 for Mie solution will not diffuse due to secondary scattering. This result can be understood from the overall energy flux conservation within the range of the particle size.

One can see in Fig. 9 new oscillations (compared to Mie solution) in the intensity distribution. In the limit of geometrical optics such oscillations present the well-know effect, Newton rings, which arise due to interference of scattered and reflected radiation. Position for the dark Newton rings can be written as (Born & Wolf, 1999):

$$\frac{m\lambda}{2} = a - \sqrt{a^2 - r_m^2}, \quad m = 1,2,... \tag{37}$$

Formally, applying this formula for a = 0.5 μm and λ = 0.266 μm one can expect the appearance of three Newton rings at r = 0.34, 0.44 and 0.49 μm.

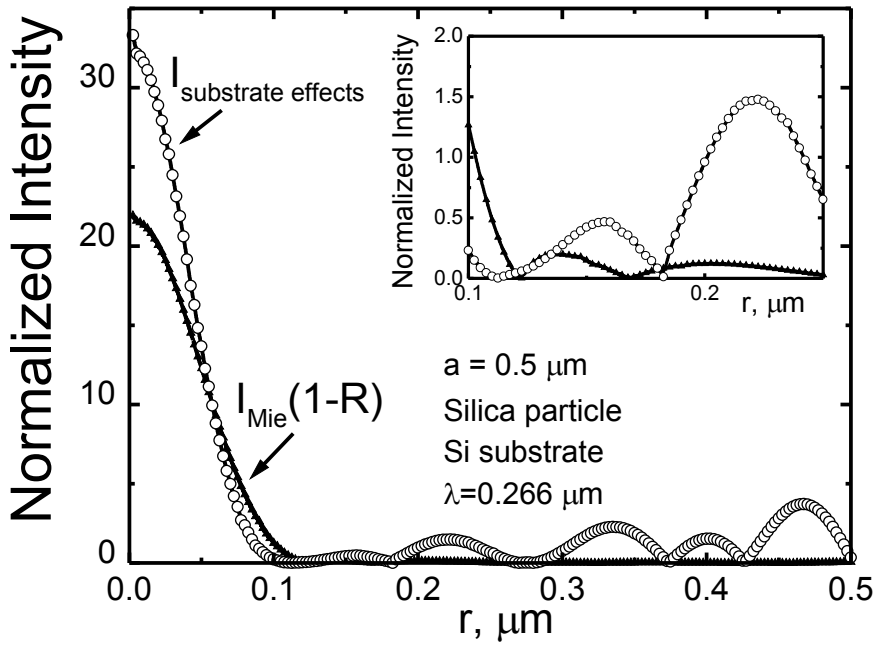

Fig. 9. Near-field light intensity along the radial axis with $\varphi = 45^{\circ}$, calculated with the Mie theory (triangular) and from reflective $\hat{\mathbf{A}}$ matrix (circles). The enhancement by the reflection of the substrate is observed near the contacting point. The ripple structure near the pedestal is shown in the insertion in the range between 0.1 μm and 0.25 μm (first two "rings").

Nevertheless, the necessary condition, $a \gg \lambda$, for formula (37) does not fulfill and this simplified consideration is not valid. Although the number of the ripples corresponds approximately to (37) some additional maximums arise. Some of these maximums exist with Mie solution (see insertion in Fig. 9) and they enhanced due to secondary scattering effects.

To analyze the origin of the sidelobe structure, we lift the particle above the substrate with a small distance δ, and examine the intensity profile on the substrate. The Newton rings should shrink inwards with increasing δ**.** The result of this examination is shown in Fig. 10. It shows that sidelobes firstly (up to the $\delta = 3$ nm) move outwards with increasing δ, which implies

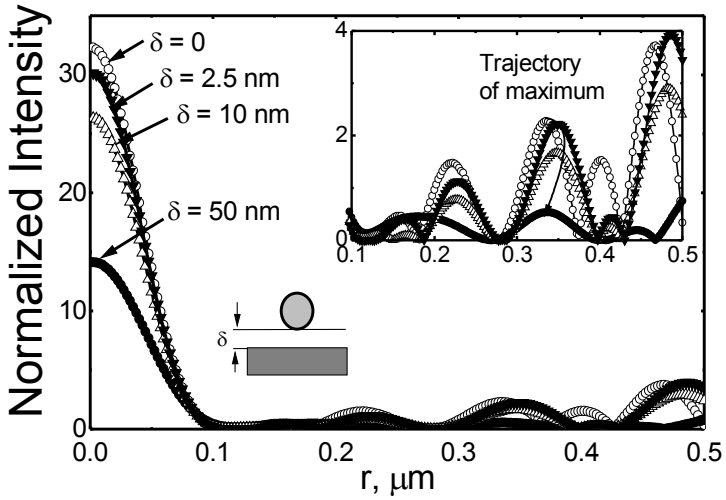

Fig. 10. Scattered light intensity on the substrate versus radial coordinate for different lifting distances δ between particle and the substrate. Light intensity drops drastically with increasing of lifting distance. The side-lobe structure shifts firstly outward with the distance, then inward. The insertion shows the trajectory of the maximum for the second "ring" is in between 0.1 μm and 0.5 μm.

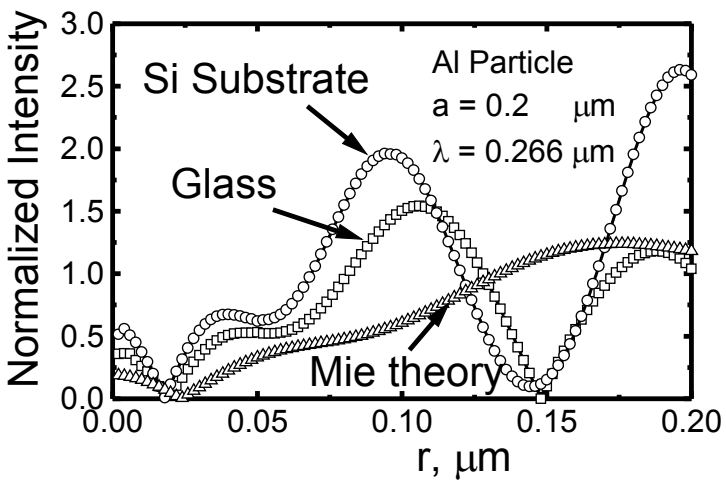

Fig. 11. Scattered light intensity in the "shadowed" area on the surface of Si and glass substrates. Higher light intensity is achieved on Si substrate due to its high reflectivity. Distribution of intensity, calculated from the Mie theory is also shown.

that the ripples are mainly due to the reflection of the near-field scattered light. Nevertheless with further increasing of δ they start to move inward. Thus we consider that this is a complex superposition of near-field Newton rings with Mie scattering. The noticeable effect is the decreasing of maximal intensity in near field region. It permits by purely optical way to measure the shift δ by the order of 1 nm! It is significantly more sensitive than the interferometric method; it is the idea for new type of microscopy.

To analyze the role of the particle and substrate materials, in Fig. 11 we present the light intensity distribution in the "shadowed" area under the aluminum particle, with two different substrates (Si and glass). The reflectivities of the two subsrates are significantly different, about 0.7 and 0.08, respectively. It is found that the near field light intensity on Si is higher than that on a glass surface. A similar effect can be responsible for the variation of the optical breakdown threshold of gas near different surfaces (Prokhorov, 1990).

One of the pecularities of the Mie solution is the typical double-peak structure in the intensity distribution for small particles, see in Fig. 4. The substrate reflection and secondary scattering can qualitatively change this picture. Due to the sharpening effect the amplification of intensity in the center is higher than at its periphery. Thus, at some range of parameters double-peak Mie structure may transfer into the single-peak structure for the particle on the surface. Calculations with MMP technique (Münzer, 2002) confirm this effect; it depends on the size parameter (see further in Section 7.1). This effect was found experimentally as well, see in Fig. 12.

4. Adhesion potential and Hamaker-Lifshitz constant

The particle is attracted to the surface by Van der Waals force, which occurs due to dipole interactions. Although the corresponding potential varies fast versus distance, as r^{-6} (Landau & Lifshitz, *Quantum Mechanics*), nevertheless, it presents the long-range interaction, e.g. contribution of this interaction to the free energy is not additive, it depends on the body shape and configuration (Lifshitz & Pitaevsky, *Statistical Physics*, Part 2). If one considers the particle as a deformed sphere, see in Fig. 13, then, according to Hamaker, 1937 the attraction force is given by

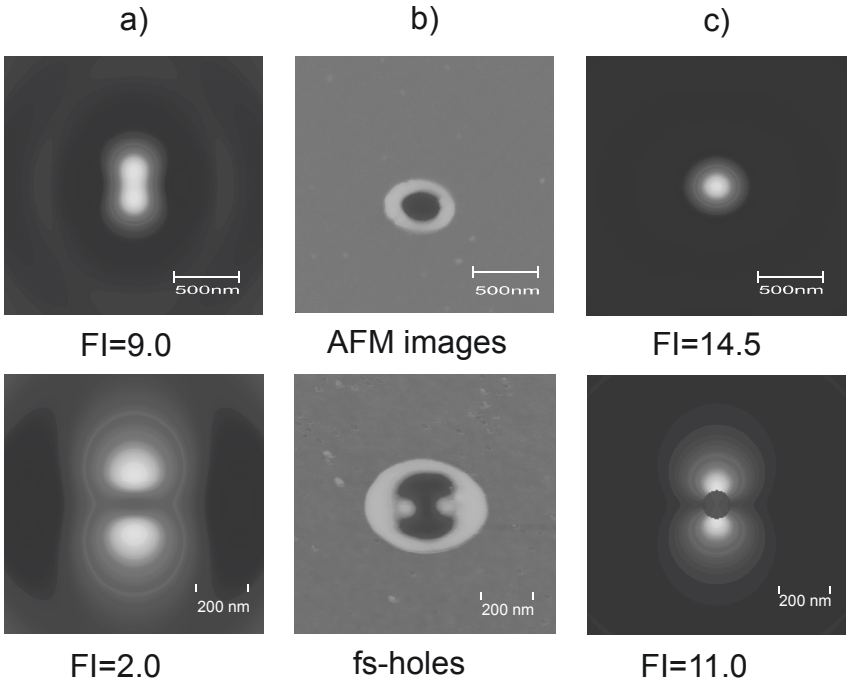

Fig. 12. Field intensity enhancement and ablation pattern underneath colloidal particles with diameters of 800 nm (top) and 320 nm (bottom) on a silicon substrate. The direction of the electrical field is orientated in the vertical direction. Calculated field enhancement by neglecting the influence of the substrate (a). Ablation pattern resulting from illumination by a fs laser pulse (experiment) (b). Calculation including the influence of the substrate (c). From Münzer, 2002.

$$F = \frac{\langle \hbar\omega \rangle a}{8\pi h^2} + \frac{\langle \hbar\omega \rangle {r_c}^2}{8\pi h^3}, \tag{38}$$

where a is radius of the particle, h is separation distance ($h \approx 4$ Å), r_c is radius of contact, The Lifshitz constant $\langle \hbar\omega \rangle$ is related to Hamaker constant A by $A = \frac{3}{4\pi}\langle \hbar\omega \rangle$. The Hamaker constant depends on the properties of the particle, substrate and medium.

This attraction force is very big; it is sufficient to say that the maximal pressure within the range of "point contact" consists, typically, of 10 Kbar and higher (Bowing, 1988). It is clear that this high loading leads to elastic or even plastic deformation of the material. Analysis of these deformations as well as the general problem of adherence is still under discussion; see, e.g. Rimai, 1995. Hertz did the first examination of pressure distribution within the contact area in 1882; this distribution follows to parabolic law:

$$P(r) = P_{max}\left(1 - \frac{r^2}{r_c^2}\right)^{1/2}, \qquad (39)$$

see analysis of the Hertz solution, for example, in § 9 in Landau & Lifshitz, *Theory of Elasticity*.

Assuming Hertzian distribution, Derjaguin, 1934 found the relation between the radius of contact, r_c, and loading force, P_ℓ, for spherical particle:

$$r_c^{\,3} = \frac{3}{4}\frac{P_\ell\, a}{E^*}, \quad \frac{1}{E^*} = \left(\frac{1-\sigma_1^{\,2}}{E_1} + \frac{1-\sigma_2^{\,2}}{E_2}\right), \quad P_0 = \frac{\langle \hbar\omega \rangle a}{8\pi h^2}. \qquad (40)$$

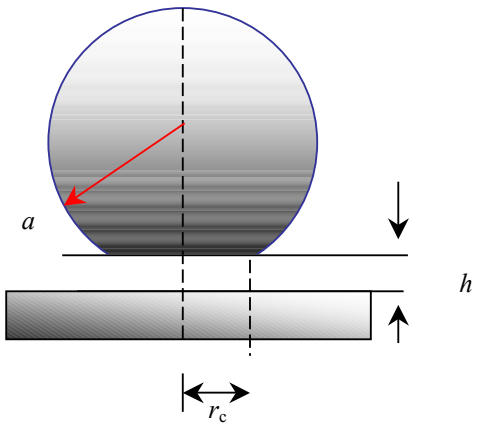

Fig. 13. Schematic for the particle on the surface. The attracting force in (38) is the result of integration with $h \ll a$ and $r_c \ll a$.

where $\sigma_{1,2}$ and $E_{1,2}$ are the Poisson coefficients and Young's modulus for the particle and substrate, without the external loading force, P_ℓ, is presented by the first term in (38). We denote this force as P_0. The adhesion-induced deformations are quite complex, and some other factors (adhesion forces outside the area of contact, etc.) should be taken into account to describe the experimental data well. At present, two models of adhesion are commonly acceptable: Derjaguin-Muller-Toropov (DMT) model for "hard" materials (Derjaguin, 1975, 1980; Muller, 1980, 1983) and Johnson-Kendall-Roberts (JKR) model for "soft" materials (Johnson, 1971, 1976). The transition between the two models was also discussed (Maugis, 1992, 1995). Without discussing the details, we want to pay attention just to the phenomena of instability, important for understanding laser cleaning. Namely, under the action of external force, *P*, the size of the contact in JKR-theory varies as (Johnson, 1976):

$$\left(\frac{r_c}{a_c}\right)^3 = \frac{P}{P_c} + 2 \pm 2\sqrt{1+\frac{P}{P_c}}, \quad a_c = \left(\frac{9\pi\gamma a^2}{4E^*}\right)^{1/3}, \quad P_c = 3\pi\gamma a, \qquad (41)$$

where γ is a surface energy per unit area (work in separating the surfaces), it includes loading due to adhesion. Sign "plus" in (41) corresponds to stable, and "minus" to unstable brunches of the solution.

One can see in Fig. 14 that applying the negative force (tensile) with the critical load $P = -P_c$ the jump-like disconnection of the particle arises. On the contrary, one can approach particle to the surface without load, but at the moment, when particle touches the surface the jump-like adhesion force arises.

This hysteresis can be seen well when the load of the particle is performed with the help of atomic force microscope (AFM), which is shown in Fig. 15. Such an experiments are very popular now to estimate the Hamaker constants, see, e.g. (Shaefer, 1995; Mizes, 1995).

The Hamaker constant is used as phenomenological parameter in the DMT and JRK theories. This constant meanwhile can be calculated from the "first principles". In the macroscopic theory, the Van der Waals interaction in a material medium is regarded as brought about through a long-wavelength electromagnetic field; this concept suggested by Lifshitz, 1955 (see also Landau & Lifshitz, *Electrodynamics of Continuous Media*)

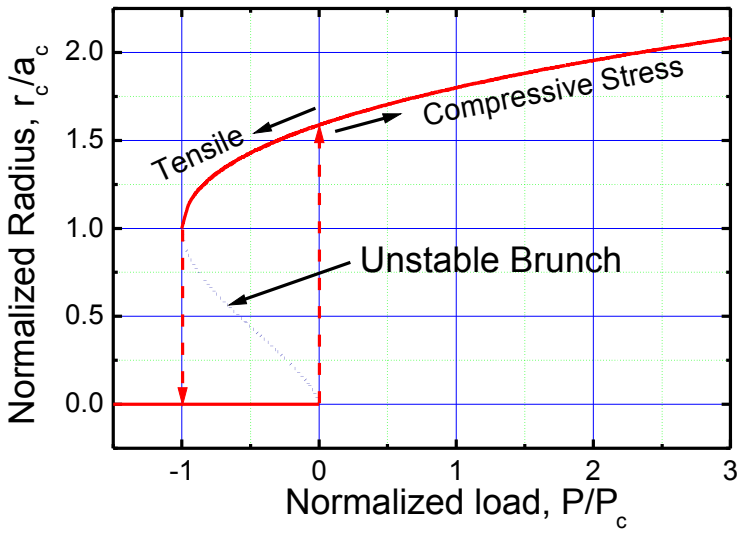

Fig. 14. Contact size-load, according to Eq. (41). In the paper of Johnson, 1976 the experimental points are shown additionally. They cover well the stable branch.

includes not only thermal fluctuations but also the zero-point oscillations of the field.

The Lifshitz theory is based on the theory of electromagnetic fluctuations developed by (Leontovich & Rytov, 1952; Rytov, 1953). Later, the Lifshitz formula was proved from the microscopic point of view, using methods of the quantum theory of field (Dzyaloshinski, 1959; 1960 a, b). The force F acting on a unit area of two bodies ("1" and "2") separated by a gap of width h, filled with a liquid (or some other substance "3") in the frame of microscopic theory is expressed through the complex dielectric constants $\varepsilon_i(\omega) = \varepsilon_i'(\omega) + i\varepsilon_i''(\omega)$, $i = 1, 2, 3$ of three materials, see e.g. monograph (Abrikosov, 1965):

$$F = \frac{A\ a}{6h^2} = \frac{\langle \hbar\omega \rangle a}{8\pi h^2} = \frac{k_B T}{\pi c^3} \sum_{n=0}^{\infty}{}' \varepsilon_3^{3/2} \omega_n^3 \int_1^{\infty} p^2 \left\{ [L_1 - 1]^{-1} + [L_2 - 1]^{-1} \right\} dp \ , \quad (42)$$

where

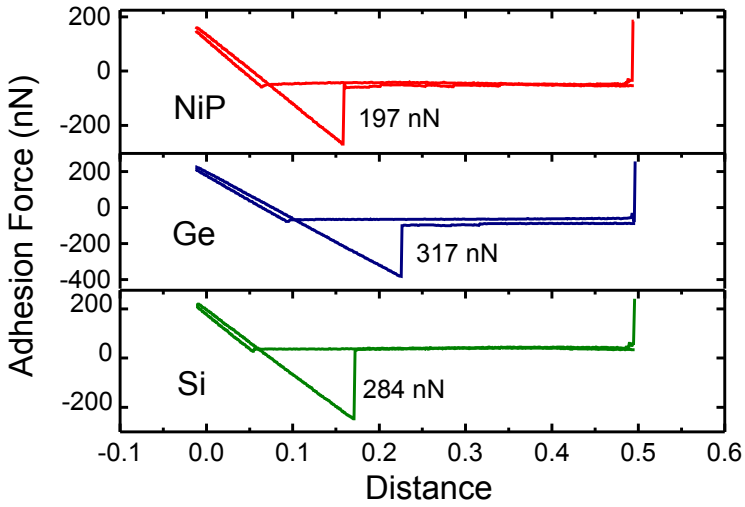

Fig. 15. AFM point-contact mode measuring the pull-off force of tip from NiP, Ge and Si substrates. The pulling force reflects different Hamaker constants of these substrates. The relative ratio of jumps is equal approximately to the ratio of corresponding Hamaker constants. Hamaker constants for Si and Ge have been reported in literature, data for NiP is original from Zheng, 2000.

$$L_1 = \frac{s_1 + p}{s_1 - p}\,\frac{s_2 + p}{s_2 - p}\exp\left[2p\sqrt{\varepsilon_3}\,\frac{\omega_n h}{c}\right],$$

$$L_2 = \frac{s_1 + p\,\dfrac{\varepsilon_1}{\varepsilon_3}}{s_1 - p\,\dfrac{\varepsilon_1}{\varepsilon_3}}\;\;\frac{s_2 + p\,\dfrac{\varepsilon_2}{\varepsilon_3}}{s_2 - p\,\dfrac{\varepsilon_2}{\varepsilon_3}}\exp\left[2p\sqrt{\varepsilon_3}\,\frac{\omega_n h}{c}\right], \qquad (43)$$

$$s_1 = \sqrt{\frac{\varepsilon_1}{\varepsilon_3} - 1 + p^2}\,,\quad s_2 = \sqrt{\frac{\varepsilon_2}{\varepsilon_3} - 1 + p^2}\,,\quad \omega_n = 2\pi n\,\frac{k_B T}{\hbar}.$$

During the summation in (42) the term with $n = 0$ should be taken with weight $1/2$, and the values of ε_1, ε_2 and ε_3 in (43) are considered as

functions of the *imaginary frequency* $i\omega_n$, i.e. $\varepsilon = \varepsilon(i\omega_n)$. When the bodies are separated by vacuum, $\varepsilon_3 = 1$.

Formula (42) can be simplified, when the temperature T is sufficiently small (change from summation to integration, see details in Lifshitz & Pitaevsky, *Statistical Physics*, Part 2). Some further simplifications can be done with the help of Kramers-Kronig relation. In the static limit, when the permittivities ε_i are replaced by their electrostatic dielectric constants ε_{i0} formula (42) can be written as (see formula (82.4) in Lifshitz & Pitaevsky, *Statistical Physics*, Part 2):

$$F = \frac{\hbar c}{32\pi^2 h^4}$$
$$\int_0^\infty dx \int_1^\infty dp \, \frac{x^3}{p^2} \left\{ \left[\frac{(s_{10}+p)(s_{20}+p)}{(s_{10}-p)(s_{20}-p)} e^x - 1 \right]^{-1} + \left[\frac{(s_{10}+p\varepsilon_{10})(s_{20}+p\varepsilon_{20})}{(s_{10}-p\varepsilon_{10})(s_{20}-p\varepsilon_{20})} e^x - 1 \right]^{-1} \right\}, \tag{44}$$
$$s_{10} = \sqrt{\varepsilon_{01} - 1 + p^2}, \quad s_{20} = \sqrt{\varepsilon_{02} - 1 + p^2} .$$

This formula was used for calculations in Lifshitz & Pitaevsky, *Statistical Physics*, Part 2. In the limit of two good metals, $\varepsilon_{10} = \varepsilon_{20} \to \infty$, the highest attraction force, F_∞, is reached (numerical number is presented for $h = 4$ Å)

$$F_\infty = \frac{\pi^2}{240} \frac{\hbar c}{h^4} \approx 0.5 \text{ Mbar} . \tag{45}$$

In Fig. 15 we present the dependence of attraction force for two identical insulators ($\varepsilon_{10} = \varepsilon_{20} = \varepsilon_0$) versus dielectric constant ε_0 in the same units as Fig. 18 in Lifshitz & Pitaevsky, *Statistical Physics*, Part 2:

$$F = F_\infty \left(\frac{\varepsilon_0 - 1}{\varepsilon_0 + 1} \right)^2 \Phi(\varepsilon_0) . \tag{46}$$

One can see in Fig. 16 that the function $\Phi(\varepsilon_0)$ varies from 1 (at $\varepsilon_0 \to \infty$) to 0.35 (at $\varepsilon_0 \approx 1$), as it was found in Lifshitz & Pitaevsky,

Statistical Physics, Part 2. This function has a shallow minimum at $\varepsilon_0 \approx 1.6$. The structure of this minimum is shown in the insertion of Fig. 16.

Another approximation for the Lifshitz constant $\langle \hbar\omega \rangle$ (or for Hamaker constant A) can be derived from (42), taking into account the first terms in the sum. For the identical materials in vacuum the Lifshitz constant is given by (see, e. g. Lee, 1990; Israelachvili, 1991):

$$\langle \hbar\omega \rangle = \hbar \int_0^\infty \left[\frac{\varepsilon'(i\zeta)-1}{\varepsilon'(i\zeta)+1} \right]^2 d\zeta \,. \tag{47}$$

Here ε' is the real part of the complex dielectric function, it can be expressed through the imaginary part, ε'', with the help of Kramers-Kronig relation

$$\varepsilon'(i\zeta) = 1 + \int_0^\infty \frac{\omega\,\varepsilon''(\omega)}{\omega^2+\zeta^2}\, d\omega \,. \tag{48}$$

The Hamaker constant was calculated from formula (47) using spectral data for many metals (see, e. g. Osborne-Lee, 1988). The simple formula for Hamaker constant follows under the approximation of the Drude theory, where the dielectric permittivity is given by

$$\varepsilon(\omega) = 1 - \frac{\omega_p^2}{\omega^2+\gamma^2} + i\frac{\gamma}{\omega}\frac{\omega_p^2}{\omega^2+\gamma^2} \,. \tag{49}$$

In the Eq. (49) ω_p is plasma frequency and γ is frequency of collisions. Substituting (49) into (48) and performing integration in (47) one can easily find

$$\langle \hbar\omega \rangle = \hbar\omega_p f\left(\gamma/\omega_p\right), \tag{50}$$

where

$$f(x) = \frac{\pi^2}{4}\frac{1}{\pi - x^2}\left\{ \frac{1}{\sqrt{\pi - x^2}}\left[\frac{\pi}{2} - ArcTan\left(\frac{x}{\sqrt{\pi - x^2}} \right) \right] - \frac{x}{\pi} \right\}. \tag{51}$$

Because for metals, typically, $\gamma \ll \omega_p$, one can use the asymptotic expansion

$$f(x) \approx \frac{\pi^{3/2}}{8} - \frac{x}{2} + \frac{3\sqrt{\pi}\, x^2}{16}, \quad \text{at } x \ll 1. \tag{52}$$

Some examples of calculations with formula (47) and (50) are shown in Table 1. The Drude parameters and optical spectra for three metals were taken from Shiles, 1980; Palik, 1985; Ordal, 1985; Qiu, 1995.

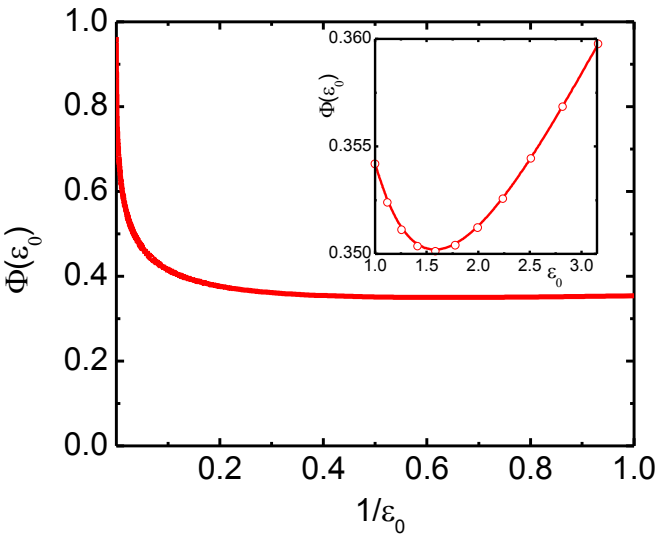

Fig. 16. Function Φ, which presents the attractive force according to Eq. (46) between two identical insulators ($\varepsilon_{10} = \varepsilon_{20} = \varepsilon_0$) versus dielectric constant ε_0.

Parameters	Al	Cu	Au
Plasma frequency, ω_p [s^{-1}]	$2.24\ 10^{16}$	$1.12\ 10^{16}$	$7.81\ 10^{15}$
Collision frequency, γ [s^{-1}]	$1.24\ 10^{14}$	$1.38\ 10^{13}$	$6.6\ 10^{13}$
Lifshitz constant, $\langle\hbar\omega\rangle$ [eV] from formula (50)	8.11	5.15	5.37
Lifshitz constant, $\langle\hbar\omega\rangle$ [eV] from the whole spectrum integration	8.59	10.7	12.3

Table 1. Calculations of the Lifshitz constant for pairs metal-metal.

One can see from Table 1 that for Al, the Lifshitz constant calculated from the approximation based on Drude theory is close to the number from the integration of the whole spectrum. However, for Cu and Au, a big

difference exists between the results that are calculated from the two methods. This difference reveals the fact that for Cu and Au, the free-electron approximation of Drude theory is not suitable for their spectrum curve, since the 3S electron of these metals exerts strong effect outside the kernel shell. Therefore to Au and Cu, the "honest" integration through the whole spectrum is preferred for calculating Lifshitz - Hamaker constant. Klimchitskaya, 2000, did the generalization of the Lifshitz formalism for the case when the spatial dispersion can be important, in addition to the frequency dependence.

With very small particles the pressure under the particle within the contact region, $P = F / \pi r_c^{\,2}$ is growing up, from equation (38) follows:

$$P = \frac{\langle \hbar\omega \rangle}{8\pi^2 h^3}\left(1 + \frac{ah}{r_c^2}\right). \tag{53}$$

Radius of contact depends on the particle radius: $r_c \propto a^{\mu}$. The value $\mu = 2/3$ follows from the DMT - model, see Eq. (40). This exponent is typical for elastic deformations. Other exponents were also discussed in the literature (Rimai, 1995). Exponent $\mu = 1/2$ is typical for plastic deformations. For elastic deformation from (53) follows the growth of the pressure with a decrease of particle size. We mentioned above that the pressure, developed under the small particle varies typically from a few tens to a few hundreds Kbar. One can expect noticeable variations in pressure, when $ah/r_c^2 \geq 0.05$. On the other hand dielectric constant ε varies with pressure, one can consider, for simplicity, a linear dependence

$$\varepsilon(P) = \varepsilon_0 + \frac{\partial \varepsilon}{\partial P} P\,, \tag{54}$$

where $\partial\varepsilon / \partial P$ can be tried as constant.

Variation in the Lifshitz constant versus ε (or dependence $P = P(\varepsilon)$ between the flat surfaces) can be estimated, e.g. from (46). What is important is that the curve $P = P(\varepsilon)$ has the "Arrhenius-like" shape. The roots of the equation are given by points where two dependences (46) and (53) are crossed. This situation is typical for Semenov diagram in the theory

of combustion (see, e.g. Karlov, 2000). Depending on the value of $\partial\varepsilon / \partial P$ coefficient equation may have one or three solutions. With higher loading pressure we have a higher ε and higher attraction force. This positive feedback may lead even to bistability in optical parameters (or in Lifshitz-Hamaker constant, or in attraction force) versus particle size.

The bistability versus particle size (or versus external loading force) looks like optical phase transition what is very attractive to use for a high-density information recording. This topic needs special discussion, which is out of the frame of the present paper.

5. Temperature under the particle

The temperature rise developed under the particle plays a decisive role for further analysis. A growth of temperature leads to thermal expansion of material, i.e. thermal deformations and stresses. Thus, we have to discuss temperature distribution within the substrate, $T = T(x, y, z, t)$, in more detail. This temperature distribution can be found from the heat equation:

$$c_s \rho_s \dot{T} = div[\kappa_s \ grad \ T] + \alpha A_0 I(x, y, t) e^{-\alpha z},$$
$$T\big|_{z=\infty} = T\big|_{x,y=\pm\infty} = T\big|_{t=0} = 0 \tag{55}$$

where surface intensity is understood as

$$I(x, y, t) = S_z(x, y) I_0(t). \tag{56}$$

Here S_z is a z-component of the Poynting vector (12) above the surface, for the unit incoming intensity and function $I_0(t)$ describes the temporal pulse shape. A_0 is the substrate absorptivity, α is the absorption coefficient and κ_s is thermal conductivity of the substrate. The problem is that distribution $S_z(x, y)$ can be sufficiently complex due to near-field focusing (see e.g. examples shown in Sections 2 and 3). One can significantly simplify the problem, considering the near-field light intensity in the symmetric Gaussian form

$$S_z(x,y) = S_0 e^{-r^2/r_0^2}, \qquad (57)$$

where r is radial coordinate, r_0 is the radius of Gaussian beam, S_0 is the field enhancement factor.

This distribution fits well the "true" distribution of near-field light intensity when latter has "one-peak" distribution. The example in Fig. 17 demonstrates the main lobe of the "true" field is quite close to the Gaussian. The contribution of intensity oscillations on the periphery (side lobes) can be ignored. The special cases where these side lobes can be important are discussed further.

The "two-peak" distribution, similar to shown in Fig. 4 can be approximated by "two-peak" Gaussian profile:

$$S_z(x,y) = S_0 \left[e^{-(x-x_1)^2/x_0^2} + e^{-(x+x_1)^2/x_0^2} \right] e^{-y^2/y_0^2}. \qquad (58)$$

For a linear heat equation the necessary solution can be presented through the Green function. For a nonlinear case, when functions c_s, κ_s, A_0 and α depend on the temperature, it needs numerical calculations and great calculation time. In the case of Gaussian profile (57) solution of linear heat equation is presented by a well-known formula:

$$T(r,z,t) = S_0 \frac{(1-R)\alpha\,\chi\, r_0^2}{2\kappa_s} \int_0^t dt_1\, I_0(t-t_1) \frac{e^{-\frac{r^2}{r_0^2+4\chi t_1}}}{r_0^2+4\chi t_1} F(z,t_1), \qquad (59)$$

where $\chi = \kappa_s / c_s \rho_s$ is the thermal diffusivity, S_0 field enhancement factor (dimensionless) and F - function is given by

$$F(z,t) = e^{\alpha^2 \chi t} \left\{ e^{\alpha z} erfc\left[\alpha\sqrt{\chi t} + \frac{z}{2\sqrt{\chi t}} \right] + e^{-\alpha z} erfc\left[\alpha\sqrt{\chi t} - \frac{z}{2\sqrt{\chi t}} \right] \right\}. \qquad (60)$$

The smooth pulse shape, $I_0(t)$, for excimer laser can be described by

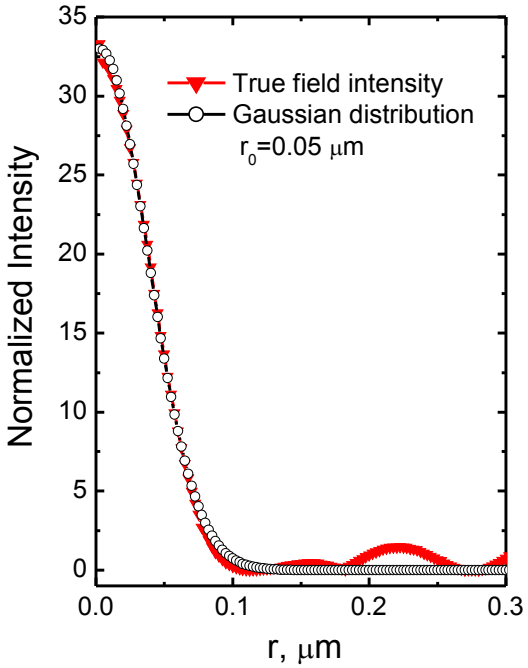

Fig. 17. The "true" intensity profile and its fitting by Gaussian beam. The "true" intensity (see in Fig. 9) presents the result of solution of the problem "particle on the surface" for 0.5 μm (radius) SiO_2 particle on the surface of Si substrate along $\varphi = 45^0$ (this presents non-polarized radiation). Radiation wavelength $\lambda = 266$ nm.

$$I_0(t) = \frac{\Phi t}{t_\ell^2} \exp\left[-\frac{t}{t_\ell}\right], \tag{61}$$

where $t_\ell = 0.409\, t_{FWHM}$ (the duration of the pulse defined at the full width at half maximum), the laser pulse energy is given by $E_\ell = \pi R^2 \Phi$, and Φ is an averaged fluence (input fluence).

Having done as many simplifications, as possible, we shall estimate the field enhancement factor S_0 from the Mie theory and then estimate r_0 value from the overall energy conservation condition. The particle geometrical

cross-section as πR^2, area of the main lobe of scattered light can be expressed as πr_0^2. The area of all the side lobes (with the same efficient "brightness" of scattering) is expressed as πr_1^2; here r_1 is effective radius. One can defines r_1 by such a way that the ratio of corresponding cross-sections will give the field-enhanced factor $S_0 = R^2/\left(r_0^2 + r_1^2\right)$. Typically, the variation of r_1 is within the limits: $0 < r_1 < r_0$. This consideration yields the following estimation for radius r_0

$$R / S_0^{1/2} < r_0 < R / 2S_0^{1/2}. \qquad (62)$$

Although it is not a strong relation, it is sufficient for estimations. In Fig. 17 one can see S_0 = 33 for r_0 = 0.05 μm. From (62) follows 0.044 < r_0 < 0.087 μm. The width of near-field focusing intensity distribution is shown in Fig. 18. It is clear that r_0 value oscillates versus the particle size. This width is typically in between 50 and 100 nm, which is very attractive for many applications.

Using values S_0 and r_0 one can estimate the temperature rise from (59). This estimation shows that maximal temperature versus particle size oscillates (see in Fig. 19). Solving linear heat equation we used parameters of Si at T = 300 K, which are presented in Table 2. In reality, the "true" temperature is higher than in Fig. 19, because the optical and thermophysical parameters of Si strongly vary with temperature. The role of temperature dependent parameters can be seen in Fig. 20, where the solution of nonlinear heat equation is presented.

Oscillations in the temperature can be more pronounced than in Fig. 19 due to secondary scattering effect, which leads to higher intensity variations, see in Fig. 7. Figure 20 b shows behaviors of 1D and 3D temperature distributions for the field enhancement, where two distributions yield approximately the same maximal temperatures. Nevertheless one can see that 3D distribution produces a faster heating and cooling.

Table 2. Parameters of Si at room temperature (300 K).

ρ_s, g/cm^3	c_s, J/(g K)	κ_s, W/(cm K)	λ, nm	α, cm^{-1}	R_0
2.3	0.72	1.23	248	1.7 10^6	0.61

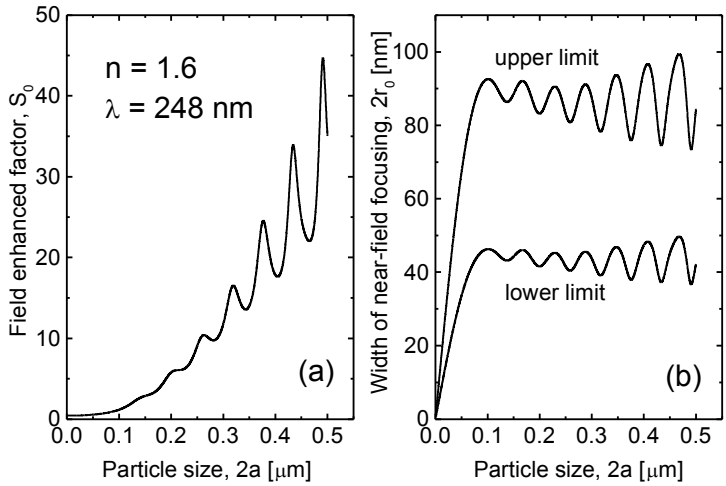

Fig. 18. Field enhancement factor, S_0 calculated from the Mie theory (a) and the width of near-field focusing (b) estimated from formula (62) for upper and lower limits. The refractive index $n = 1.6$ and the radiation wavelength $\lambda = 248$ nm.

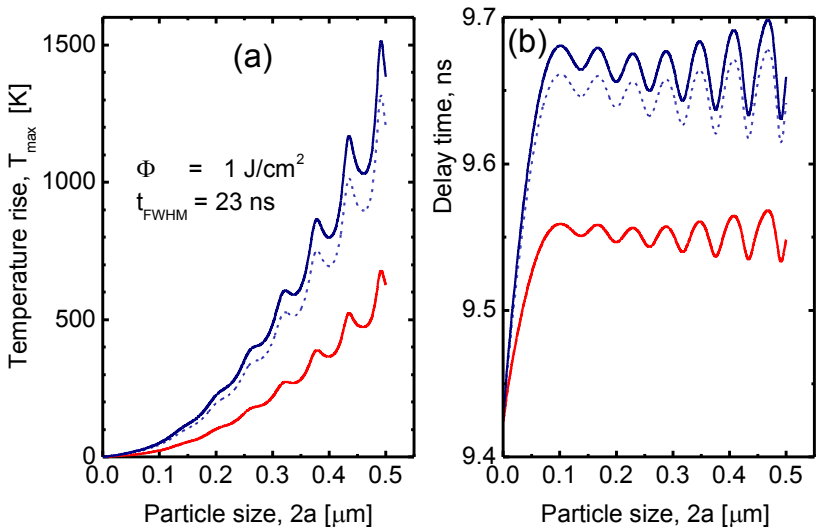

Fig. 19. (a) Maximal temperature, under the particle. (b) Delay time, when temperature reaches its maximal value (b). Field enhancement factor, S_0, and r_0 values are taken from Fig. 19. Two solid curves correspond to upper and lower limits in Fig. 19 b. The dash curves are calculated for $\kappa = 1.42$ W/cm K. Laser pulse width, t_{FWHM} = 23 ns and fluence $\Phi = 1$ J/cm^2.

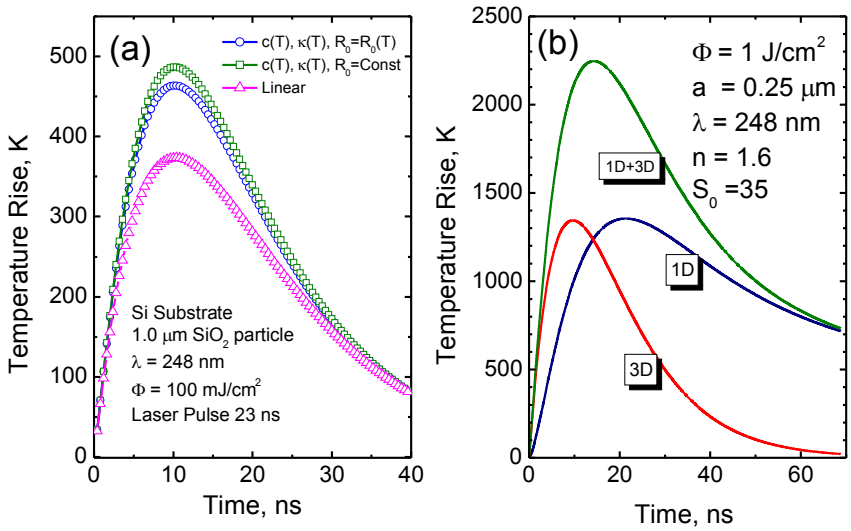

Fig. 20. (a) Temperature profile at the central point under the particle, calculated with non-linear heat equation by finite difference method (FDM) (Ozisik, 1994). Solution of linear heat equation yields the lowest maximal temperature. (b) Comparison of 3D (with field enhancement effect) and 1D solutions (without field enhancement) of linear heat equation.

In reality, the temperature under the particle is influenced by complex distribution of intensity, see e.g. Fig. 4 or Fig. 9. This distribution consists of 3 parts: 1) out of particle at $r > a$ it tends to homogeneity 1D intensity I_0; 2) in the region of enhanced radiation at $r < r_0$ it tends to enhanced field intensity $S_0 I_0$; 3) in the region of "shadow", $a < r < r_0$, intensity is rather small. One can neglect oscillations within the shadow region and the particle edge, and approximate the total intensity distribution by a sum of three Gaussian distributions (see in Fig. 21):

$$I(r,t) = I_0(t)\left[1 + S_0 e^{-r^2/r_0^2} - e^{-r^2/a^2}\right], \qquad (63)$$

where $r_0 = a/\sqrt{S_0}$, this provide conservation of energy. We shall call this simplified distribution (63) as "1D + 3D heat model". An example of the calculation of the temperature rise with this model is shown in Fig. 20 b.

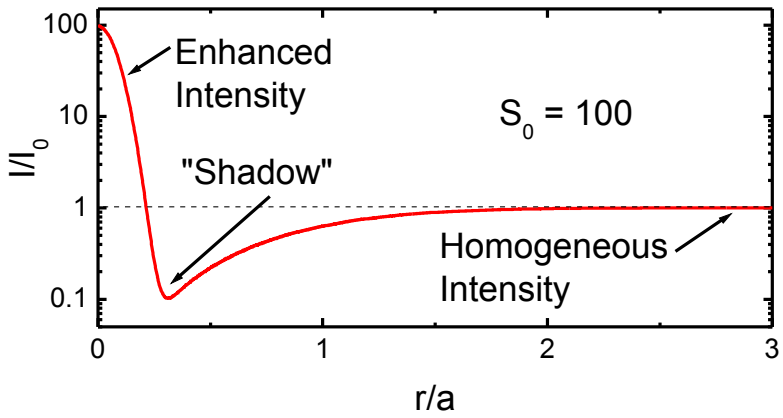

Fig. 21. Schematic for the intensity distribution on the substrate surface under the transparent particle. It can be approximated by the sum of three Gaussian distributions (63).

6. Dynamics of the particle, 3D effects

A particle on the surface performs its motion in the field of adhesion potential, which consists Van der Waals attraction and elastic forces. When the temperature is smaller than the melting temperature, then the main cleaning effect of laser action is related to material thermal expansion.

When the substrate expands, the position of the substrate surface, z_s, varies with time, $z_s = z_s(t)$, $z_s(0) = 0$. The particle displacement is a function of time t, say $z = z_f(t)$. Then the varying deformation parameter, $\delta(t)$ at time t can be expressed as

$$\delta(t) = z_s(t) + z_p(t) - z_f(t) + \delta_0 . \qquad (64)$$

Here term $z_p(t) = \alpha_T^{(p)} a T_s(t)$ describes the effect of the particle heating due to thermal contact. We assume that the temperature of the particle is the same as the substrate surface temperature, $\alpha_T^{(p)}$ is the *linear* thermal expansion coefficient for the particle (we use additional superscript

to distinguish the particle and substrate materials). If no external load acts on the particle, the initial deformation parameter δ_0 is expressed in DMT theory by

$$\delta_0 = \frac{1}{8}\left[\frac{9a\langle\hbar\omega\rangle^2}{2\pi^2 h^4 E^{*2}}\right]^{1/3}, \quad \frac{1}{E^*} = \left(\frac{1-\sigma_p^2}{E_p} + \frac{1-\sigma_s^2}{E_s}\right), \tag{65}$$

where $\sigma_{p,s}$ and $E_{p,s}$ are the Poisson coefficients and Young's modulus for the particle (index "p") and substrate (index "s"), $\langle\hbar\omega\rangle$ presents the Lifshitz constant.

The acceleration due to the elastic force can be expressed (Lu, 2000) by:

$$\frac{4}{3}\pi a^3 \rho_p \frac{d^2 z_f(t)}{dt^2} = \frac{4}{3}\sqrt{a}\, E^*\left[\delta(t)^{\frac{3}{2}} - \delta_0^{\frac{3}{2}}\right], \tag{66}$$

where ρ_p is the density of the particle and we neglect the energy losses due to plastic deformations and sound generation (Luk`yanchuk, 2001; Arnold, 2002). When the substrate expands, the position of the substrate surface, z_s, varies with time, $z_s = z_s(t)$. This expansion is the driving force for dry laser cleaning. The initial conditions for Eq. (66) are

$$\frac{dz_f}{dt}\Big|_{t=0} = \frac{dz_p}{dt}\Big|_{t=0}, \quad z_f\big|_{t=0} = 0. \tag{67}$$

The surface position, $z_s(t)$, is given by the z-component of the vector of displacement, $\mathbf{u} = \mathbf{u}(x, y, z, t)$ at z = 0. To find this displacement vector one should solve the equation of thermal elasticity (Landau & Lifshitz, *Theory of Elasticity*; Sokolnikoff 1956):

$$\rho_s \ddot{\mathbf{u}} = \frac{E_s}{2(1+\sigma_s)}\Delta\mathbf{u} + \frac{E_s}{2(1+\sigma_s)(1-2\sigma_s)}\mathbf{grad}\, div\ \mathbf{u} - \frac{\alpha_T^{(s)} E_s}{(1-2\sigma_s)}\mathbf{grad}\, T\ , \tag{68}$$

where $\alpha_T^{(s)}$ is the *linear* thermal expansion coefficient for substrate and $T = T(x, y, z, t)$ is the temperature distribution within the substrate.

The solution of the equation (68) for the stationary problem (laser beam with Gaussian intensity distribution) was presented in Welsh, 1988. This solution is valid for the calculation of the stresses and strains. Nevertheless displacement, e.g. u_z - component, which follows from this formal solution, contains logarithmic divergence, related to $1/r$ spatial distribution of the stationary thermal field at big distances (Arnold, 2002). Meanwhile, it is clear that the stationary limit is senseless, i.e. in the real physical situation the corresponding integrals should be cut off, and such calculations were presented recently (Luk`yanchuk, 2001). Nevertheless the cutting procedure is not strictly defined and it is more precise to use nonstationary solution (Luk`yanchuk, 2002 a, b). For different estimations we shall use parameters, listed in Table 3.

Parameter	Values for different materials			
	Si	Ge	NiP	SiO_2
Absorption Coefficient [cm^{-1}]	$1.7\ 10^6$	$1.6\ 10^6$	$5.7\ 10^5$	1
Absorptivity	0.39	0.35	0.71	0.95
Density [g/cm^3]	2.3	5.33	8.9	2.2
Thermal Conductivity [W/cm K]	1.42	0.73	0.14	0.0146
Heat Capacity [J/g K]	0.72	0.31	0.54	0.74
Melting Temperature [K]	1685	1210	1200	1873
Young Modulus [$dynes/cm^2$]	$1.3\ 10^{12}$	$8.2\ 10^{11}$	$2.0\ 10^{12}$	$7.3\ 10^{11}$
Poisson Ratio	0.28	0.3	0.31	0.18
Linear Thermal Expansion [K^{-1}]	$2.6\ 10^{-6}$	$6.0\ 10^{-6}$	$12.0\ 10^{-6}$	$0.54\ 10^{-6}$
Hamaker Constant, A, [J]	$2.5\ 10^{-19}$	$3.1\ 10^{-19}$	$1.2\ 10^{-19}$	$0.5\ 10^{-19}$
Lifshitz Constant, $\langle \hbar\omega \rangle$, [eV]	6.54	5.18	3.14	1.32

Table 3. Parameters used in the calculations (taken at T = 300 K). Optical parameters are given for λ = 248 nm (KrF excimer laser). Hamaker constant is given for the pair of identical materials, i.e. Si-Si, etc. Data for Hamaker constant (or Lifshitz constant) are taken from Bowing, 1988; Visser, 1972; Heim, 1999.

a) *1D model*.

This case is the simplest. We use solution $T = T(z, t)$ of 1D heat equation. From this solution one can estimate the surface displacement by

$$z_s(t) = 2(1+\sigma_s)\alpha_T^{(s)} \int_0^\infty T(z,t)dt \ . \qquad (69)$$

The additional multiplier $2(1+\sigma_s)$ in (69) appears when one considers the "quasi-1D approach", where displacements and stresses are considered to be equal zero at infinity (at *x-y* plane). This term without a detailed explanation was written in Prokhorov, 1990; Vicanek, 1994. The detailed examination of the thermal elasticity problem, which precisely introduces this term, is given in Arnold, 2002. For the "true" 1D problem multiplier $2(1+\sigma_s)$ is absent. Experiment of Dobler, 1999, where corresponding displacement and accelerations were measured experimentally, was closer to "true" 1D problem rather than "quasi-1D approach".

Because of the energy conservation, one can write condition

$$A \int_0^t I(t_1)dt_1 = c\rho \int_0^\infty T(z,t)dz \ , \qquad (70)$$

here c and ρ are heat capacity and density of the heated substrate respectively, A is absorptivity of the surface. If one considers a smooth pulse shape (61), then for the displacement holds the following formula:

$$z_s(t) = 2(1+\sigma_s)\frac{\alpha_T^{(s)} A\Phi}{c\rho}\left[1-\left(1+\frac{t}{\tau}\right)e^{-t/\tau}\right]. \qquad (71)$$

For the rectangular laser pulse with the pulse duration τ_ℓ, a similar dependence is given by

$$z_s = 2(1+\sigma_s)\frac{\alpha_T^{(s)} A\Phi}{c\rho}\left[\frac{t}{\tau_\ell}\Theta_H\left(1-\frac{t}{\tau_\ell}\right)+\Theta_H\left(\frac{t}{\tau_\ell}-1\right)\right], \qquad (72)$$

here $\Theta_H(x)$ is the unit step function (Heaviside function). Pay attention that the rectangular pulse produces infinite accelerations at $t=0$ and $t=\tau_\ell$.

The 1D model has natural restriction, related to absence of inward motion of the surface during cooling stage. To take into account this effect one should use the 3D thermo-elastic model. Effects related to temperature

dependencies of parameters (solution of non-linear heat equation) can also play important role.

Although the heating process happens only within a short time interval, it determines both the kinetic energy and the elastic potential energy necessary to overcome the adhesion force.

Condition for the particle removal can be written from the energetic consideration Lu, 2000:

$$\frac{8}{15}E^*\sqrt{a\,\delta(t)^5}+\frac{4}{3}\pi a^3\frac{\rho v^2}{2}\geq\frac{1}{2}P_\ell\,\delta(t)+\frac{\langle\hbar\omega\rangle a}{8\pi h}. \qquad (73)$$

Here v is understood as a relative velocity: $v=\dot{\delta}(t)$. Another condition is the so-called "force criterion", which follows from (66) and (40) at quasi-static conditions:

$$-\frac{4}{3}\pi a^3\rho_p\ddot{z}_f=\frac{4}{3}\sqrt{a}\,E^*\left[\delta_0{}^{\frac{3}{2}}-\delta(t)^{\frac{3}{2}}\right]\geq\frac{\langle\hbar\omega\rangle a}{8\pi h^2}. \qquad (74)$$

Pay attention that the force criterion needs necessary condition $\ddot{f}<0$, i.e. it works just on the stage of particle deceleration. The transition between the two (force and energy) criterions was discussed in Arnold, 2002.

An example of solution is shown in Fig. 22. The pulse shape with fluence 1 J/cm^2 and dynamics of the surface temperature rise $T_s = T_s(t)$ are shown in Fig. 22 a. The pulse duration is considered to be 23 ns, and the initial temperature is $T_\infty=300\,K$. Maximal surface temperature reaches 1561 K, which is close to Si melting temperature T_m = 1685 K. With higher fluences we exceed the melting temperature.

Different components of the deformation parameter (64) are shown in Fig. 22 b. The expansion, related to the thermal expansion of the particle is very small, $z_p \ll z_s$, mainly due to the small value of the particle's thermal expansion coefficient, $\alpha_T^{(p)}$. Deformation parameter δ oscillates with amplitude ≈ 1.5 Å around the equilibrium value $\delta_0 \cong 3$ Å. For the SiO_2 particle with a = 0.5 μm used in calculations, period of oscillations consists ≈ 6.4 ns. It is approximately 20 times longer than the period of the first

mode of the particle sound vibration, $T_p = 4a / u_s$ (Landau & Lifshitz, "*Theory of Elasticity*"), where $u_s = 5.5 \cdot 10^5$ cm/s is sound velocity in quartz. We do not take into account these "high frequency" sound vibrations. We also neglect damping in "low frequency" oscillations. In principle, this damping occurs due to sound generation (Arnold, 2002) and due to plastic deformations in the particle-substrate contact area (Luk`yanchuk, 2001). Oscillation dynamics in dry laser cleaning was suggested in Luk`yanchuk, 2001, 2002 a, b; Arnold, 2002. This dynamics permits resonant enhancement.

Fig. 22 c presents characteristic velocities: $v_s = \dot{z}_s$, $v_p = \dot{z}_p$, $v_f = \dot{z}_f$ and $\dot{\delta}$. Although the condition $z_p \ll z_s$ is fulfilled for all interesting parameters of laser cleaning with 248 nm radiation and SiO_2 particles on the Si surface, velocities of expansion can be comparable, e.g. for 5 μm particles near the cleaning threshold, $v_{s\max} \approx 2 v_{p\max}$.

Fig. 22 d presents characteristic accelerations: $a_s = \dot{v}_s$, $a_p = \dot{v}_p$, and $a_f = \dot{v}_f$. Maximal accelerations due to substrate surface expansion can be smaller than maximal accelerations produced by particle heating, i.e. $a_{p\,max} \gg a_{s\,max}$. It holds for the big particles. The dash line presents the critical acceleration for the "force criterion":

$$a_c = -\frac{3}{24\pi^2} \frac{\langle \hbar\omega \rangle}{\rho_c a^2 h^2}. \qquad (75)$$

With fluence 1 J/cm^2 $\ddot{\delta}$ is close to reach this critical value. The "energy criterion" (73) presents a line on the plane of parameters $\{\delta, \dot{\delta}\}$. When the phase trajectory of the system crosses the line, the condition for the particle removal is fulfilled (see in Fig. 23). The "energy criterion" yields higher threshold fluence than those, which follow from the "force criterion". For small particles with $a \leq 1$μm the removal occurs mainly due to big deformations δ.

With bigger particles kinetic energy starts to play an important role: phase trajectory touches the energy criterion curve at the point with non-zero value of velocity $\dot{\delta}$.

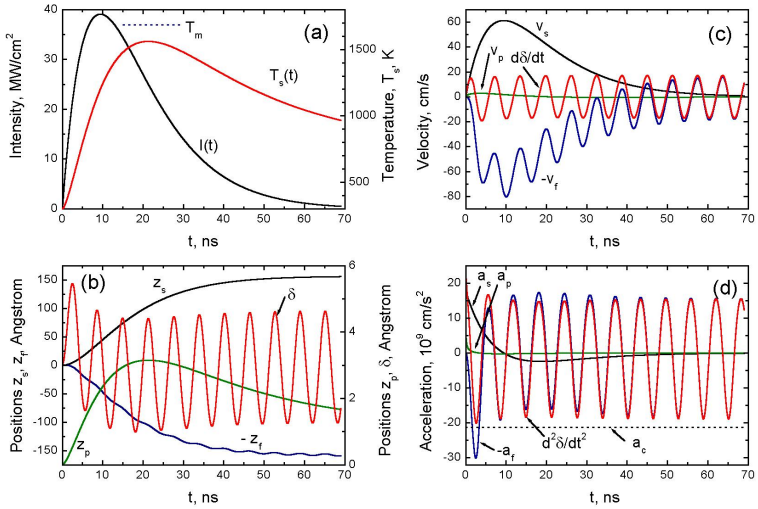

Fig. 22. Dynamics of dry laser cleaning for 1μm SiO_2 particle on Si surface: a) laser pulse shape and the surface temperature for laser pulse length 23 ns and fluence 1 J/cm^2; b) different components of displacement and deformation in accordance with (64); c) characteristic velocities: $v_s = \dot{z}_s$, $v_p = \dot{z}_p$, $v_f = \dot{z}_f$; d) characteristic accelerations: $a_s = \dot{v}_s$, $a_p = \dot{v}_p$, and $a_f = \dot{v}_f$. Value a_c corresponds to critical acceleration, which follows from the "force criterion" (74).

Although 1D model explains qualitatively behavior of the threshold fluence versus particle size, it yields threshold fluences by the order of magnitude higher than the experimental (see in Fig. 24). It means that some important physics is missing with 1D model.

Another discrepancy is related to minimal size of the particle, which can be removed in dry laser cleaning. 1D model predicts the minimal size $2a \approx 1\,\mu\text{m}$ (a smaller size needs a surface temperature above the melting temperature). Meanwhile many groups reported about cleaning efficiency up to the size 0.2 μm in dry laser cleaning. Within the frame of 1D model there are no oscillations in threshold fluence, related to optical resonance.

b) *3D model*.

To find the surface position, $z_s(t)$, we have to use solution of 3D heat equation and solution of 3D thermal elasticity problem (see in Appendix A Chapter 2). We assume the Gaussian distribution (57) for the near-field

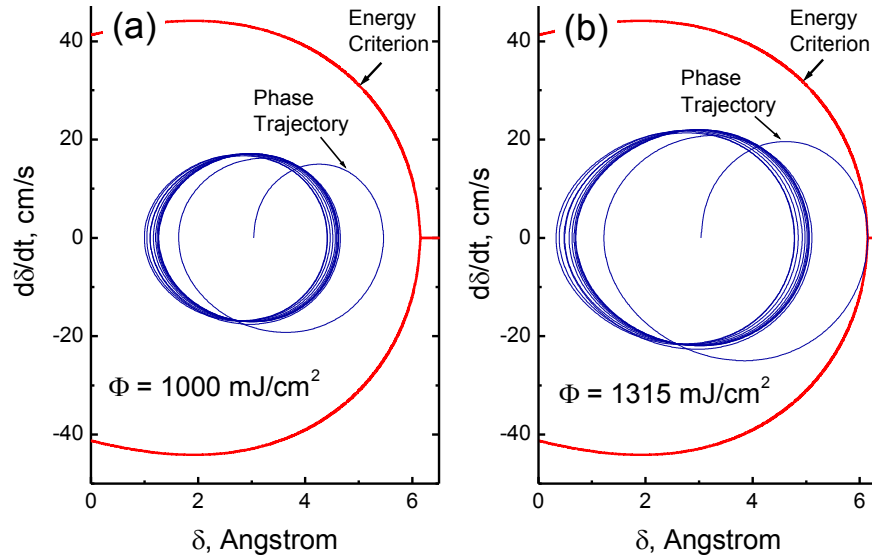

Fig. 23. Energy criterion curve, calculated from (73) and phase trajectory calculated from integration of (66), (67). Particle size is 1μm. Pictures (a) and (b) correspond to different laser fluences.

light intensity, $I(r,t)=I(t)e^{-r^2/r_0^2}$. Then in the center of the laser beam we have:

$$z_s(t)=u_z=2\,\alpha_T^{(s)}\,(1+o_s)\,\frac{A\,r_0^2\,\alpha\,\chi}{\kappa}\int_0^t dt_1 I(t-t_1)\frac{2}{r_0^2+4\chi t_1}\int_0^\infty dz_1\left[1-\sqrt{\pi}\varsigma\, e^{\varsigma^2}\,erfc\varsigma\right]F(z_1,t_1), \tag{76}$$

where $\varsigma=z_1/\sqrt{r_0^2+4\chi t_1}$, and F- function is given by formula (60). Solving the Newton equation (66) for the particle motion in elastic potential with driving force (76) one can see the main peculiarities of the particle dynamics with 3D model (see in Fig. 25).

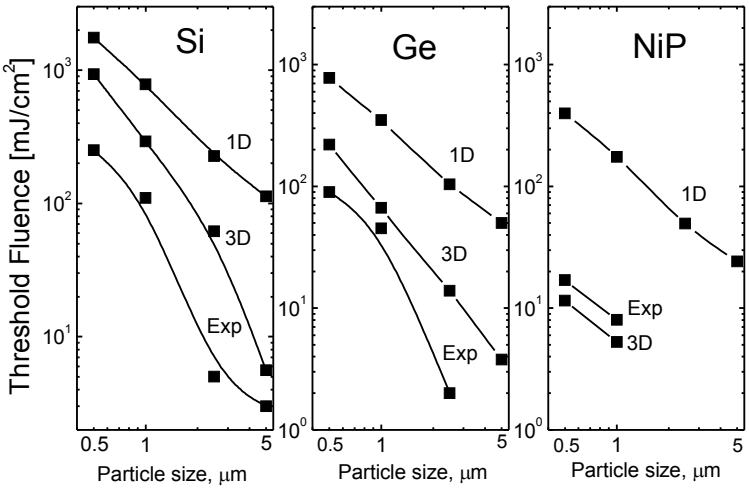

Fig 24. Theoretical (for 1D and 3D models) and experimental results of the threshold laser fluences for SiO_2 particles versus particle size for Si, Ge and NiP substrates. Excimer laser λ = 248 nm, pulse duration 23 ns.

Although 3D expansion with the same intensity yields smaller z_s values than 1D expansion, it is faster. As a result characteristic deformation velocities and accelerations can be comparable or even greater than in 1D case. The calculations shows that the threshold fluence for 3D model with a = 1 μm typically by the order of magnitude smaller than for 1D model (see in Fig. 24).

Further improvement in the position of theoretical curve can be done with 1D + 3D model. This model considers the distribution of laser intensity, given by (63). Surface expansion is a combination of results given by formulae (71) and (76).

With growth of the particle size the enhancement factor oscillates and possible maximum values becomes higher (see in Fig. 7). For example, with a = 1 μm, λ = 248 nm and n = 1.6 the nearest maximum yields S = 343. It is clear that such high degree of the enhancement factor will be limited by the particle surface quality and it shapes deviation from the ideal sphere.

Silicon substrate is a particular material with a strong temperature dependences of optical and thermophysical parameters. It needs solution of nonlinear heat equation. One can see in Fig. 20a that the nonlinearities yield a higher surface temperature. The same effect produces combination of 1D

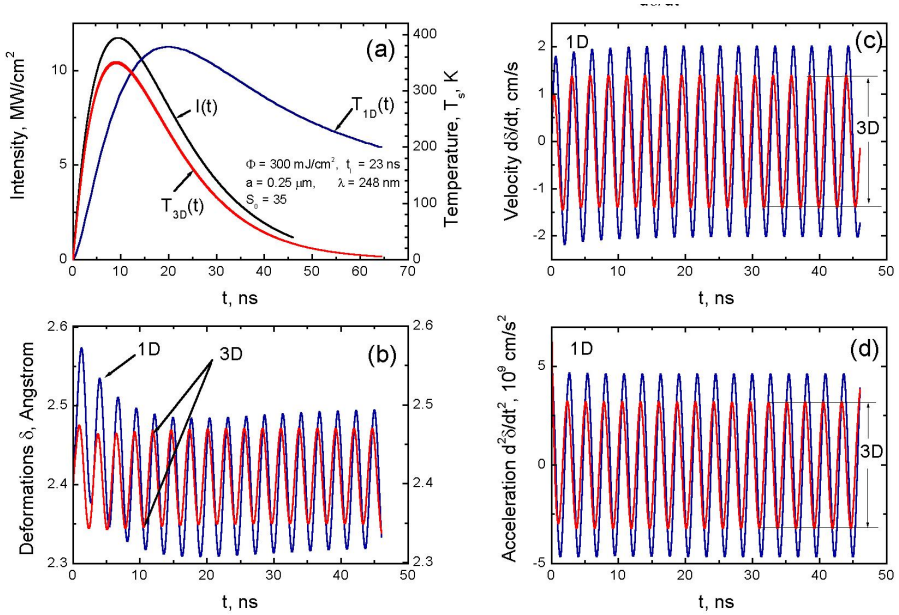

Fig. 25. Substrate expansion and particle movement for SiO_2 particle on the Ge substrate. Laser fluence is 19.2 mJ/cm^2. Enhanced near-field light intensity is modeled as Gaussian beam with a radius of 0.1 μm. a) Laser intensity, $I(t)$ and corresponding 1D and 3D temperature dynamics. Combined 1D+3D case is shown as well. b) Displacements z for the particle (p) and substrate (s) for 1d and 3D heating. c) particle displacement $f(t)$ for 1D and 3D heating and d) corresponding particle velocities.

and 3D model compared to 3D model (see in Fig. 20b). Both effects move the theoretical curve into the "correct direction" i.e. closer to experiment but we did not analyze the nonlinear problem in more detail.

The different cleaning efficiencies of 1.0 μm silica particle from Si, Ge and NiP surfaces were examined, see in Fig. 26. It is found that the laser cleaning efficiency increases sharply along with the laser fluence. For 1.0 μm particles, threshold laser fluences exist at about 100 mJ/cm^2 for Si, about 30 mJ/cm^2 for Ge, and about 8 mJ/cm^2 for NiP substrate. It is also concluded that particle removal from NiP is the easiest in the three substrates, while removal from Si is the most difficult.

Comparing the physical parameters of the materials, see in Table 3, one can see the Van der Waals force of particles on Ge is the greatest of the three substrates, while the adhesion force on NiP is only about 2/3 of Ge. However, particle removal is related not only to the adhesion force, but also to the optical and thermal properties of the substrates. For Si, the absorptivity and thermal expansion coefficients are much less than for Ge and NiP. Therefore higher laser fluence is required to remove particles from Si substrate. Removal from NiP is the easiest, not only because the adhesion force is the least of the three substrates, but also because its absorptivity and thermal expansion coefficients are much greater than the other substrates. The small thermal conductivity of NiP also contributes to its low threshold, since the real heating process is more analogous to "pointing heating" due to the near-field effect. This experiment demonstrates that substrate thermal expansion certainly plays an important role in dry laser cleaning mechanism.

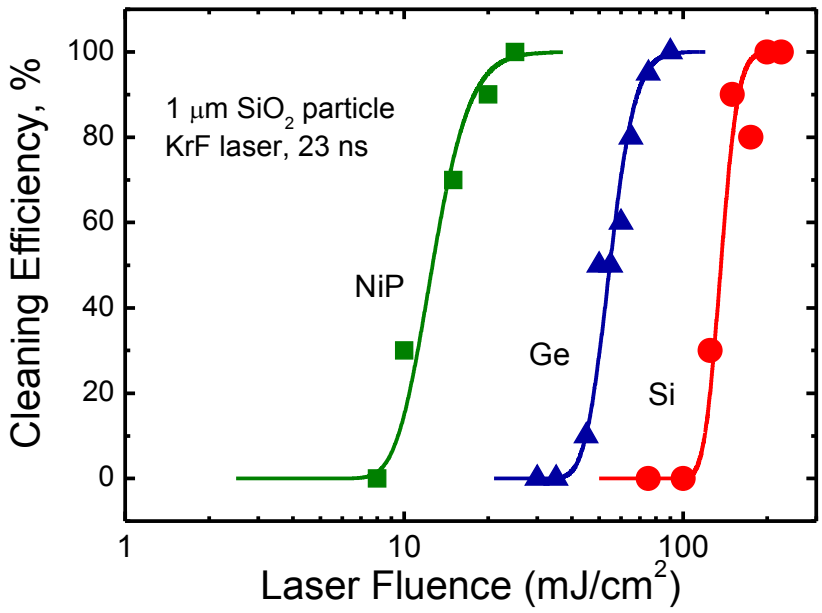

Fig. 26. Cleaning curves for NiP, Ge and Si substrates (from Zheng, 2001).

Nevertheless the 1D thermal expansion model consistently yields values, which are by one-two orders of magnitude higher than experimental data (see in Fig. 24). At the same time 3D model yields values much closer to experiment. For example, for NiP substrate 3D model practically coincides with experiment. Pay attention that 3D effects in heating and deformation play an important role of for both, transparent and absorbing particles.

7. Comparison with experimental results

In this section we will discuss experimental findings that allow a verification of the theoretically predicted intensity enhancement in the near field of particles resting on a surface. Besides their interest from a fundamental point of view, these experiments are of great importance for applications such as laser cleaning of particles on surfaces.

7.1. Local substrate ablation – a probe for optical near fields

Clearly, any conclusive evidence for the presence of intensity enhancement in the near field of particles at surfaces should rely on directly accessible experimental facts. Indirect indications such as the removal of particles at lower laser fluences than predicted by theory (Lu, 2000a) can be considered as a hint, however, they strongly rely on the correctness of the respective theory.

The most common approach for probing near fields at small particles is the application of Scanning Near Field Optical Microscopy (SNOM) (Durig, 1986). Although this is a well-established technique it inevitably disturbs the field distribution around the particle by the presence of the probe itself.

We therefore chose a new and different approach in order to probe undisturbed near field distributions as were found in laser cleaning applications (Leiderer, 2000; Lu 2000c, 2002; Münzer, 2001; Mosbacher, 2001; Münzer, 2002; Huang, 2002 a, b). In this approach we use the substrate, that is already present anyway, as the imaging medium, and consequently do not rely on the introduction of an additional probe into the field. Surface modifications due to structural transitions, defects formation, oxidation, melting or evaporation that are induced by the intensity

enhancement at the enhanced laser intensity can be detected by optical, electron or scanning probe microscopy.

7.1.1 Morphology of near field-induced damage sites

Typical examples for such modification sites are shown in Fig. 27. In order to clearly relate any observed modification to the former particle sites, we have marked the initial positions of the colloidal spheres by evaporating a thin (10 nm) SiO_2 layer onto the sample after application of the colloidal particles and before the laser irradiation (Leiderer, 2000). After the application of the laser pulse the particles have been removed, and the sample was inspected in a Scanning Electron Microscope (SEM). As can be seen from Fig. 27 a), the particles size and their position could be determined by a contrast in the SEM pictures due to the different thickness of the oxide layers in and outside the particle site. By a comparison of the hole diameters on wafers with and without the additional oxide layer we have checked that this layer did not influence the optical properties of the particles.

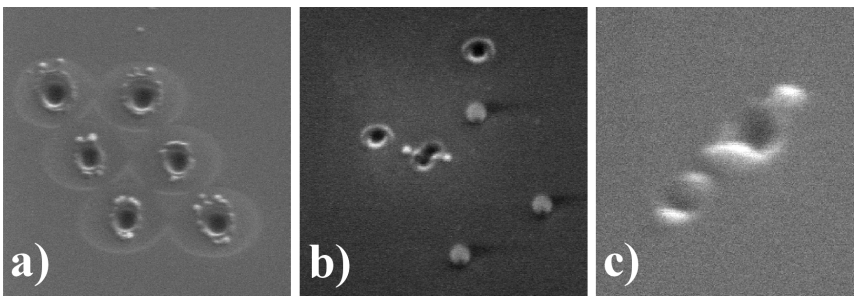

Fig. 27. Holes generated due to local field enhancement at laser-irradiated particles on a silicon wafer. In 27 a) and 27 b) the particles were PS spheres with a diameter of 1700 and 320 nm, respectively; in 27 c), irregular alumina particles with an average size of 400nm were used. The side lengths of the displayed squares are 6800 nm, 4970 nm, and 1300 nm for a), b) and c), respectively (from Leiderer, 2000).

The displayed image represents a shadowgraph of a cluster of six particles, which were removed. At the center of each particle a hole was created, just at the positions where the numerical calculations predict the highest laser intensity. Similar holes were found also for smaller particles (see Fig. 27 b). The laser used here had a FWHM of 150 fs and a wavelength of λ = 800 nm. By the choice of this short pulse length we minimized the heat diffusion in the silicon substrate and made sure that any ablation pattern reflected the actual intensity distribution at the particle.

As it turned out in all experiments where we removed particles by laser irradiation with ps and fs pulses, this removal was always accompanied by the appearance of such holes. Hence the particle removal – or "cleaning" process can be directly related to the ejection of material from the wafer, which then also leads to the observed crater formation. One might argue that realistic contaminants that have to be removed by laser cleaning applications are typically not of spherical shape. Also for irregular contaminants such as Al_2O_3 powder, however, field enhancement takes place – but in contrast to the spherical particles in asymmetric patterns – giving rise to the generation of holes also. An example of such a structure is shown in Fig. 27 c).

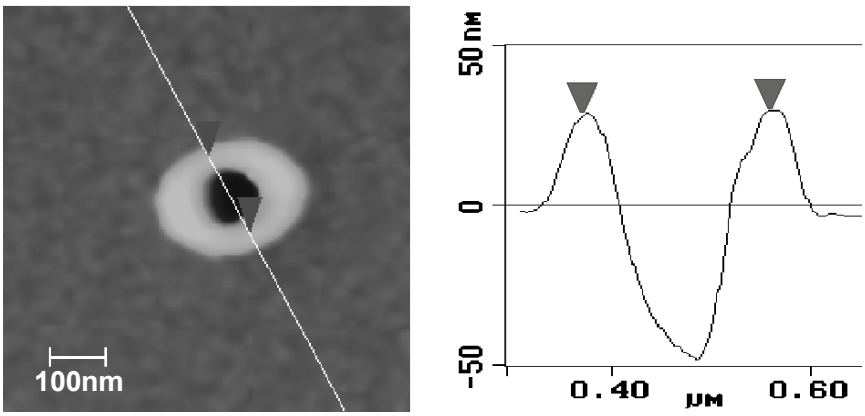

Fig. 28. AFM image of a singe hole created by irradiation of a 370 nm PS sphere with laser pulses from a frequency doubled Ti: Sapphire-laser (λ = 400 nm) (from Münzer, 2002)

While in laser assisted particle removal the generation of holes due to local substrate ablation is an undesired, defect creating process, it may as well be utilized for nanolithographic surface structuring purposes (Leiderer, 2000; Lu, 2000c, 2002; Münzer, 2001; Münzer, 2002; Huang, 2002 a, b). By controlled application of a colloidal suspension, deposition of isolated PS spheres at any desired concentration onto the substrate is possible. Such isolated spheres can be used to create single holes. An example is shown in Fig. 28. In order to decrease the hole's size, the illumination wavelength was decreased to 400 nm and particles with a diameter of 370 nm have been illuminated. AFM imaging of the holes created this way reveal a hole diameter of about 100 nm – about one quarter of the applied laser wavelength or even one eight's part of the wavelength (Huang, 2002a).

An exciting possibility besides the fabrication of single holes is the exploitation of self-organization processes, e.g. the utilization of 2-D colloidal monolayer, for the structuring process (Burmeister, 1998). Illumination of an array of particles by an ultrashort laser pulse leads to an

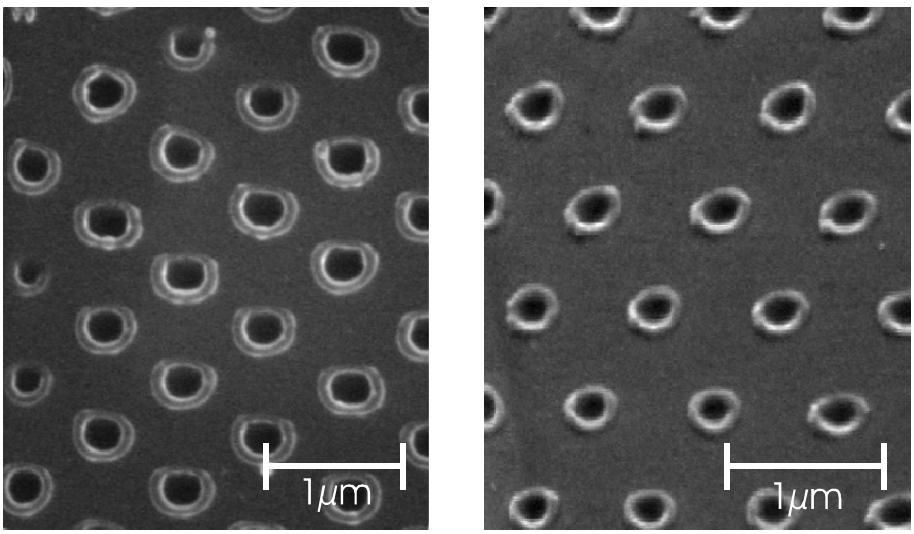

Fig. 29. Hole arrays formed after illumination of a hexagonal colloidal monolayer with fs (FWHM= 150 fs, λ=800 nm) laser pulses. Left: silicon substrate, right: germanium substrate (from Münzer, 2002).

array of holes. This is shown in Fig. 29 where hexagonal monolayer of polystyrene spheres arranged on silicon and germanium substrates have been used to create hexagonal hole patterns. Being a parallel technique this method allows the structuring of large substrate areas and can result in a million holes and more for a single shot, limited only by the size of the laser spot. A similar technique was used to produce nanosize patterning in metallic films shown in Fig 30 (Huang, 2002 a, b). It was demonstrated that ns excimer laser produced a lattice of holes with a size below 50 nm (using 140 nm PS particles, see in Fig. 31).

7.1.2. Parameters influencing field enhancement induced ablation

As already discussed above, the laser pulse length considerably influences the morphology of the field enhancement induced defect patterns in the substrate. Whereas laser pulses with FWHM in the ps and sub-ps range lead to well-pronounced ablation patterns, nanosecond laser pulses lead to a completely different defect shape. An SEM image of such a shallow, broadened melting pool is shown in Fig. 32.

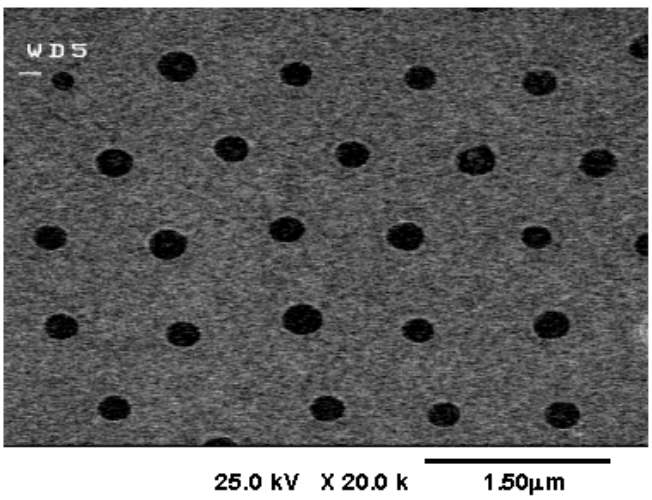

Fig. 30. SEM image of periodic pit arrays formed after illumination of isolated 1.0 µm SiO_2 particles on an Al film surface by a single laser pulse (FWHM = 23 nm, λ = 248 nm) with a laser fluence of 300 mJ/cm^2 (from Huang, 2002 a, b).

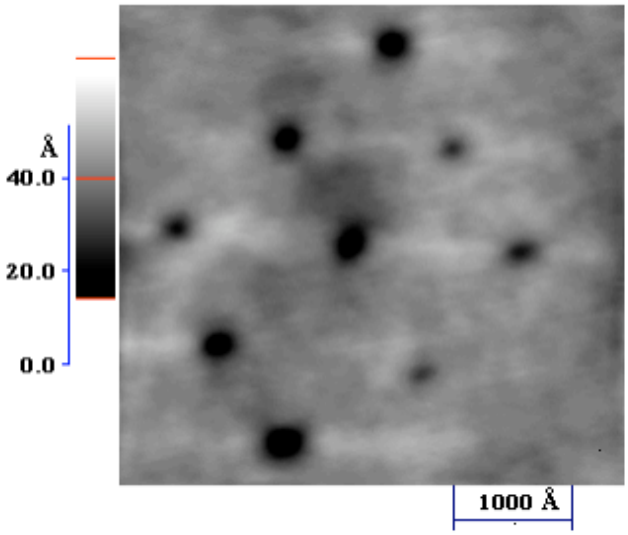

Fig. 31. SEM image of periodic pit arrays formed after illumination of isolated 140 nm polystyrene particles on an Al film surface by a single laser pulse (FWHM = 23 nm, λ = 248 nm) with a laser fluence of 300 mJ/cm^2 (from Huang, 2002). The smallest holes are of diameters ≈ 300 Å (from Huang, 2002 a).

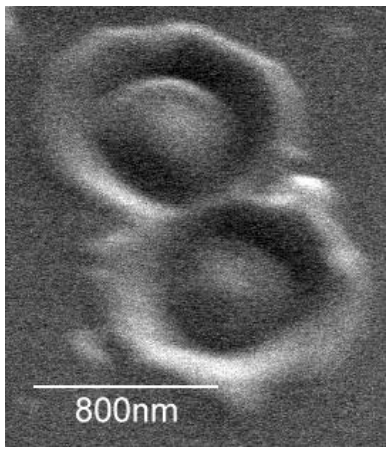

Fig. 32. Scanning electron microscope image of a typical melting site induced by field enhancement after ns laser illumination. In comparison to fs laser induced hole structures the morphology of the damage site is clearly smeared out due to heat diffusion in the silicon substrate (from Mosbacher, 2002).

Another parameter that might influence the field enhancement process considerably is the presence of the substrate itself. It was pointed out (Luk`yanchuk, 2000), that in numerical calculations the intensity is increased by a factor of 1.5 as a consequence of the presence of a silicon substrate. Also the calculations based on the 3D model in the above sections strongly suggest, that the substrate should have a major influence on the process.

Motivated by these predictions we have conducted a set of experiments that allow the imaging of the actual field distribution at particles *on* surfaces and compared these experimental findings to calculations for free space (purely Mie-theory) and calculations including the substrate. The results of this comparison are shown in Fig. 12.

Neglecting the influence of the substrate we computed on the basis of the Mie theory the field of polystyrene particles in the substrate plane by an algorithm taken from Barber, 1990. The patterns resulting from these calculations are shown in Fig. 12a for a 320 nm (bottom) and an 800 nm (top) particle illuminated by a plane wave with a wavelength of 800 nm. They exhibit a double-peak structure with a distance between the maxima of about 300 nm for both particle sizes, whereas the absolute value of the intensity enhancement differs by a factor of 4.5.

In a next step we compared these calculations to the experimental results shown in Fig. 12b. As previously shown (Münzer, 2001), fs laser irradiation of particles on surfaces creates an ablation pattern underneath each illuminated particle. For constant laser fluences, all sites of ablation exhibit the same morphology. Underneath particles 320 nm in diameter, the ablation pattern shows a double hole structure, yet the distance between the maxima is obviously smaller than for the free space calculation. The pattern formed underneath an 800 nm particle does not show two peaks at all, but exhibits an elliptical shape.

Apparently, the Mie calculations differ substantially from the experimental findings. However, this theory holds only for an illuminated sphere in free space, thus neglecting the influence of the substrate. Consequently, these differences can be attributed to the influence of the silicon surface on the field distribution (see above in the Section 3).

In order to investigate this in more detail we performed semianalytical field calculations using the Multiple Multipole (MMP) technique (Hafner, 1990). Advantage was taken of the mirror symmetries of the problem and ring multipoles (were used to model the scattered fields both in the substrate

and in vacuum). Optical constants were taken from Palik, 1998. The result of these calculations is shown in Fig. 12c. The calculated field distributions fit the experimental findings well, if for the particles 800 nm in diameter we compare them to the results obtained in the substrate (10 nm below the surface) and for the smaller particles with those above (10 nm above the surface). The reason for this needs some further investigation. Besides the effect of ablation in the central part of the hole one observes the formation of a rim around the ablated area. In the development of this rim structure the dynamics of the melt influenced by viscosity and surface tension may play a role.

7.2. Near-field effects in the laser cleaning process

The above-described experimental results clearly show the importance of near field effects for the field of laser cleaning. In the following will illustrate these consequences.

7.2.1. Experimental details

For dry laser cleaning we determined the removal efficiency and the cleaning thresholds in laser fluence for contaminants of different sizes and materials. We deposited individual spherical colloidal polystyrene[1] (PS) on industrial silicon wafers in a spin coating process described in Mosbacher, 2002b. Prior to particle application the wafers were cleaned in an ultrasonic bath in isopropanol (IPA). The samples prepared in this way were irradiated by a single Nd: YAG laser pulse (λ = 532 nm, FWHM = 8 ns) either in ambient conditions (relative humidity 30-40%) or in high vacuum (HV, 10^{-6} mbar). In ambient cleaning a flow of pressurized, filtered air was used to blow away the removed particles and to prevent their redeposition.

Under ambient conditions particle removal in the cleaned area (about 1 mm^2) was detected by a light scattering technique (Mosbacher, 2000). A 5 mW HeNe laser illuminated a spot with a diameter of 0.5 mm, which corresponds to several hundred particles monitored, its scattered light was detected by a photomultiplier. The monitored area was much smaller than the illuminated area, therefore in this case the laser fluence can be

[1] IDC, Portland, Oregon, USA

considered as almost homogeneous. In HV we determined the fluences necessary for particle removal by inspecting the illuminated spot with an optical microscope prior and after the laser pulse. We measured the threshold cleaning fluence relatively to the melting threshold of Si, monitoring the reflected light of the HeNe laser with ns time resolution. As the laser fluence for the onset of melting of silicon is well known, this can be used for a conversion of relative fluences into absolute numbers.

7.2.2. Variation of the size parameter

Within the frame of the Mie theory the extent of intensity enhancement in the near field of the particle critically depends on the size parameter $q = \pi d/\lambda$, where d denotes the particle diameter and λ the applied wavelength. When the secondary scattering of reflected radiation is taken into account (see Section 3) both parameters d and λ influenced independently. Experimentally there exist two approaches of varying q parameter in laser cleaning experiments, either by changing the particle size or by varying the wavelength. We will discuss both in the following.

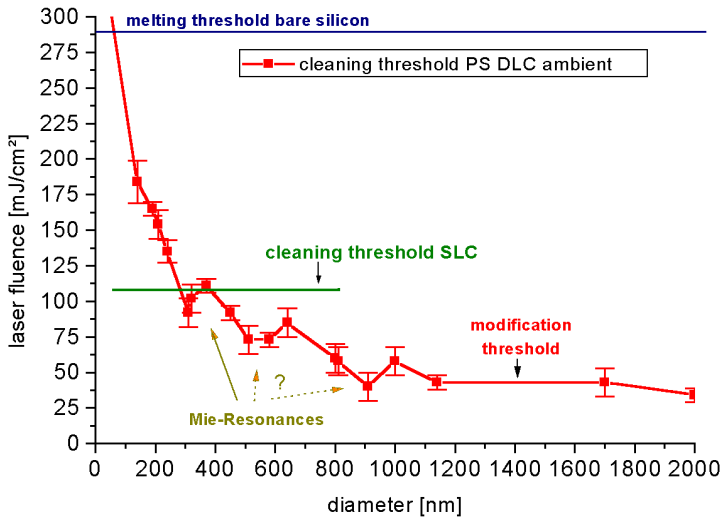

Fig. 33. Threshold in the applied laser fluence for particle removal in DLC in ambient air. Particles smaller in diameter than 110 nm could not be removed (from Mosbacher, 2002a)

7.2.2.1. Variation of the particle size

First we have studied particle removal in ambient conditions. This environment represents the conditions that may be found in a possible future application of the process.

In Fig. 33 the thresholds in applied laser fluence for the removal of PS particles are plotted as a function of the particle size. From this diagram one can obtain a lot of information on the process, especially on the role of field enhancement.

First we would like to bring to mind two very important thresholds in the laser cleaning process. One of them is the threshold for the onset of melting of the bare substrate. As dry laser cleaning is aimed for an industrial application, any change of the structure of the silicon wafer, i.e. the silicon substrate and a native oxide layer of specified thickness, as induced by melting has to be strictly avoided. From experiments (Kurz, 1983; Lowndes, 1983; Boneberg, 1993) this melting threshold is known to be about 280 mJ/cm^2, which therefore represents the upper limit of applicable laser fluence. The second threshold, also indicated in Fig. 32, is the cleaning threshold of the steam laser cleaning process. In previous investigations (Mosbacher, 2000) we found this threshold to be independent of the particle diameter (60-800 nm) and material (PS, SiO_2, Al_2O_3).

In order to obtain information on the dependency of the cleaning threshold on the particle size we investigated many different particle diameters in the range of 110-2000 nm.

At first sight the shape of the curve follows an r^{-k} – trend, where r denotes the particle radius and $1 < k < 2$. This *monotonic* behavior was predicted theoretically (Bäuerle, 2000), and in fact already the first publications on dry laser cleaning reported that smaller particles are harder to remove than larger ones (Zapka, 1991a; Tam, 1992; Engelsberg, 1993). If one looks closely, however, one discovers additionally an *oscillating* behavior of the threshold fluences as function of the particle diameter. This is illustrated in Fig. 33 by the line connecting the data points and reflects the resonant enhancement of the incoming laser intensity in the near field of the particles.

However, it should be pointed out, that the line connecting the data points is just a guide to the eye and does probably not describe the exact field enhancement efficiency as function of the particle diameter. The number of the discrete particle sizes used in our experiments is not

sufficient to resolve this dependency. Nevertheless the resonances account for the deviation of the curve from a smooth, monotonic shape.

Besides decreasing the applied laser fluence necessary to remove particles, field enhancement underneath the particles is responsible for surface damage by local melting/ablation of the substrate, as shown in Section 7.1. Depending on the pulse length used for the cleaning laser, and hence the thermal diffusion length during this laser pulse, local ablation leads either to the formation of steep holes (ultrashort pulses <100 ps) or shallow melting/ablation sites (nanosecond pulses).

In dry laser cleaning using ultrashort pulses the removal of a particle is always accompanied by the formation of a hole, i.e. the hole formation threshold is identical with cleaning threshold. Consequently in this case the particles are removed by the momentum transfer of the ablated species rather than by thermal substrate expansion – local ablation acts as a cleaning mechanism (Mosbacher, 2001). This shows very clearly that for a damage free dry laser cleaning ultrashort pulses are not suitable.

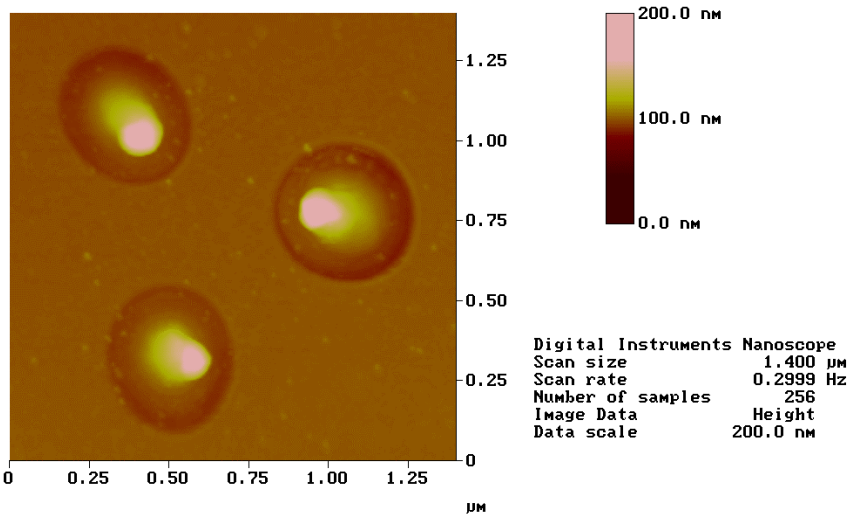

Fig. 34. Atomic force microscopy (AFM) image of a damage site after dry laser cleaning using ns pulses. The damage site was created by an agglomerate of three PS spheres 800 nm in diameter. Note the typical damage morphology: a shallow trench surrounds a central hillock (from Mosbacher, 2002 and 2002c).

Against this background also for the case of ns pulses we focused our interest on the determination of the *local melting/ablation* thresholds in addition to the cleaning thresholds. Instead of the melting threshold of the bare silicon surface this damage threshold represents the true upper limit for the applicable laser fluence and is by its nature particle dependent. For the determination we made use of the Gaussian spatial beam profile of our cleaning laser. Due to this profile a spatial variation in the cleaned area corresponds to a variation in the locally applied laser fluence. In a post process analysis we investigated the cleaned areas of our samples with an AFM. By this method we imaged the field enhancement induced damage sites (cf. Fig. 12 for an SEM image), a typical example can be seen in Fig. 34.

Imaging damage sites at different locations in the cleaned areas and especially at their borders, which correspond to the cleaning threshold fluence, we determined the damage threshold for each particle size. For all particles investigated the cleaning threshold was identical with the damage threshold. Damage free dry laser cleaning was *not* possible applying the laser parameters we used!

The AFM images contain even more information on the particle removal mechanism as they reveal quantitative topographic information. All the investigated damage sites showed the same features: a “trench” surrounded a central “hillock”. Generally spoken the hillock was lower at high laser fluences and the trench deeper, for low laser fluences a hillock was detectable but the trench almost disappeared. In Fig. 35 we have plotted in a double logarithmic graph the mean trench depths for the investigated particles for damage that occurred at the cleaning/damage threshold.

This plot clearly shows two regimes: for particles smaller than about 250 nm in diameter the depth remains almost constant at about 1 nm. For larger particles we found a strong increase in the trench depth, the volume of the hillock was smaller than that of the trench – ablation had taken place.

From this observation we conclude, that even for dry laser cleaning using *nanosecond* pulses local ablation of the substrate plays a role as cleaning mechanism for “large” particles where the field enhancement is higher and thus provides fluences high enough for ablation. At smaller particles field enhancement probably causes local melting, but no ablation.

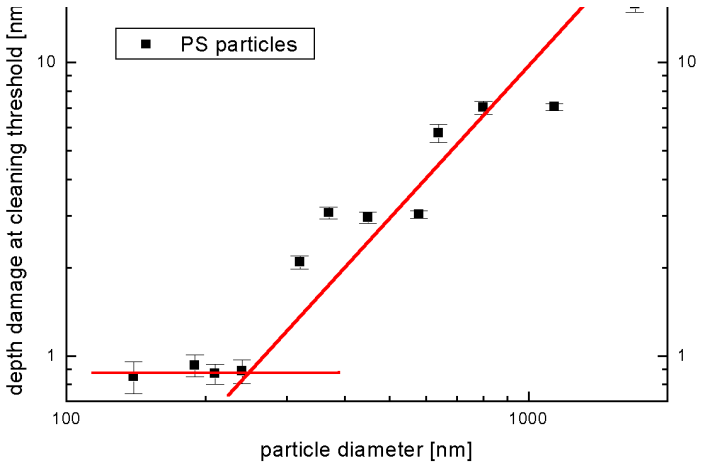

Fig. 35. Trench depth of the damage sites as a function of the particle size when the particles were removed in DLC applying the threshold cleaning fluence. For particles larger than 250 nm in diameter the depth increases strongly with the particle size, for smaller particles it remains almost constant (from Mosbacher, 2002 and 2002c)

7.2.2.2. Variation of the laser wavelength

A doubtless probing of the optical resonances in dry laser cleaning is not possible by a variation of particle sizes, as they are available only in certain, discrete diameters. On the contrary, it is possible to vary the laser wavelength continuously using an optical parametrical oscillator (OPO). For our dry laser cleaning experiments we chose a wavelength interval from 500 nm to 630 nm. It contains the wavelength of the frequency doubled Nd: YAG laser (532 nm) used in the previous experiments, and the refractive index of silicon – one parameter that influences the field distribution at the particle - does not vary too much in this wavelength range.

In Figure 36 we show the experimental results for the wavelength-dependent cleaning thresholds of particles with diameters of 370, 400 and 450 nm, respectively. The laser wavelength was varied in steps of 5-10 ± 0.2 nm, comparable to the standard deviation of the particle diameter size distribution. As the optical properties of the silicon substrate vary in the wavelength interval used, we have plotted the cleaning threshold in the

absorbed laser energy as function of the size parameter, i.e. the incident laser intensity was corrected by the wavelength dependent reflectivity.

Taking a look at the results for the particles 370 nm and 450 nm in diameter, one can see that the absorbed energy per area necessary for particle removal decreases with increasing size parameter (corresponding to decreasing laser wavelength). This can be ascribed to the higher absorptivity of silicon at smaller wavelengths, which facilitates particle removal via field enhancement induced local ablation.

The same overall trend is present for the particles 400 nm in diameter, as well. However, at a size parameter of 2.3 – 2.4 a plateau can be observed which reflects the expected *non-monotonous* dependence of the cleaning threshold on the size parameter in the presence of a *resonant* enhancement of the incoming laser radiation.

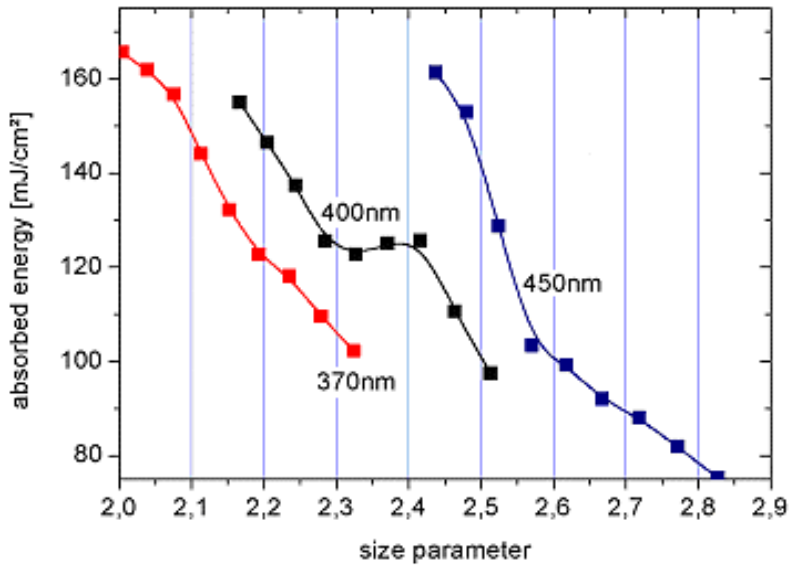

Fig. 36. Variation of the dry laser cleaning threshold as function of the size parameter when the laser wavelength is varied (from Mosbacher, 2002d).

7.2.3. Influence of the incident angle

Usually in laser cleaning studies the samples to be cleaned are irradiated at an incident angle perpendicular to the substrate surface. Consequently, the

maximum intensity of the laser light due to field enhancement is located right underneath the particle in the substrate surface plane. Especially for particles larger in size than the wavelength, where the field enhancement pattern is quite similar to a "point-focus" known from geometrical optics, the location of this maximum intensity is crucial for the cleaning performance as it leads to the local surface ablation.

A deviation from the perpendicular incidence results in a displacement of the maximum field intensity away from the contacting point. Such a displacement should result in a drop in the cleaning efficiency, and indeed this could be confirmed experimentally (Zheng, 2001). Silicon samples with particle contamination (SiO_2, diameter 2.5μm) on the surface have been irradiated by a KrF excimer laser (FWHM ≈ 23 ns, λ=248 nm) at incident angles ranging from 0°-30°. The incident laser fluence of 43 mJ/cm² was chosen well above the cleaning threshold fluence of about 5 mJ/cm², which should result in a complete particle removal. However, as the experimental results displayed in Figure 37 show, this is not the case for incident angles different from 0°. On the contrary, the efficiency decreases with increasing incident angel, and for angles above 15° no particle removal was detected.

Besides the cleaning efficiency we plot the uniform laser intensity as function of the incident angle. This intensity is proportional to $A(\theta)cos\,\theta$, where θ is the incident angle, and A is the absorptivity. The variation of incident angle from 0^o to 15^o causes the effective laser fluence to drop less than 3.5% (see in Fig. 37) – negligible in comparison with the efficiency drop.

From the calculation based on the Mie theory (Zheng, 2001) follows that the near-field light intensity in agreement with the experimental results declines from 100% to zero, when the tilting angle increases from 0^o to 15^o.

7.2.4. Influence of the surface roughness

Another nontrivial consequence of near field focusing can be found from the dependence of the cleaning efficiency on the surface roughness. The roughness by itself leads to a decrease in the Hamaker force because of a smaller contact region. The theoretical prediction shows that due to this the particle adhesion force drops with the presence of very small roughness (Whitehouse, 1970; Schaefer, 1995; Soltani, 1995). It was confirmed

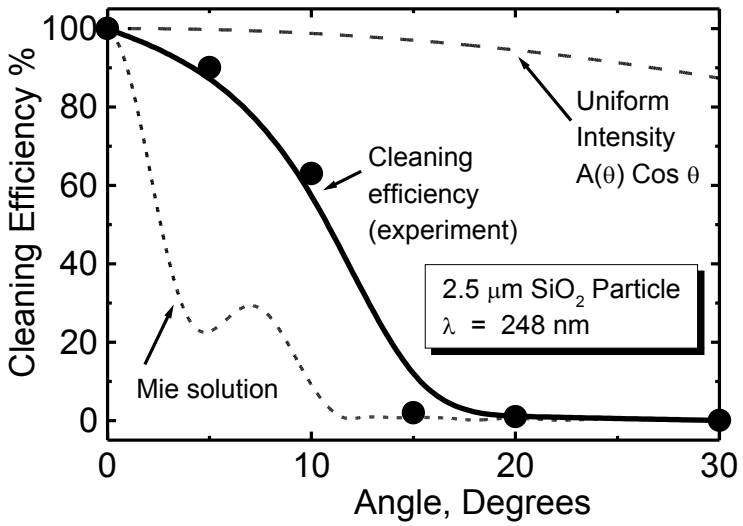

Fig. 37. Cleaning efficiency versus incident angle (from Zheng, 2001). The uniform light intensity and the Mie solution are nornalized to 100 % at normal incidence.

experimentally in static experiments with AFM (Schaefer, 1995). At the same time the roughness leads to a "lifting" of the particle above the surface, which results in a fast decrease in the near-field light intensity. Roughness amplitude of 50 nm reduces the laser intensity by a factor of two (see in Fig. 10). Thus, in spite of the reduction of the Hamaker force, one should expect a decrease of cleaning efficiency due to fast decrease of laser intensity with particle lifting.

The cleaning curves for different samples (with different roughness amplitude) are shown in Fig. 38. The SiO_2 particle size was 1.0 μm. One can clearly see decrease in the cleaning efficiency versus surface roughness.

8. Conclusion

The theory of dry laser cleaning, based on 1D thermal expansion of the substrate was the dominant model for the last 10 years. This theory predicts qualitatively correct results; nevertheless it yields the quantitative discrepancy with experiment by one-two orders of the magnitude. One can

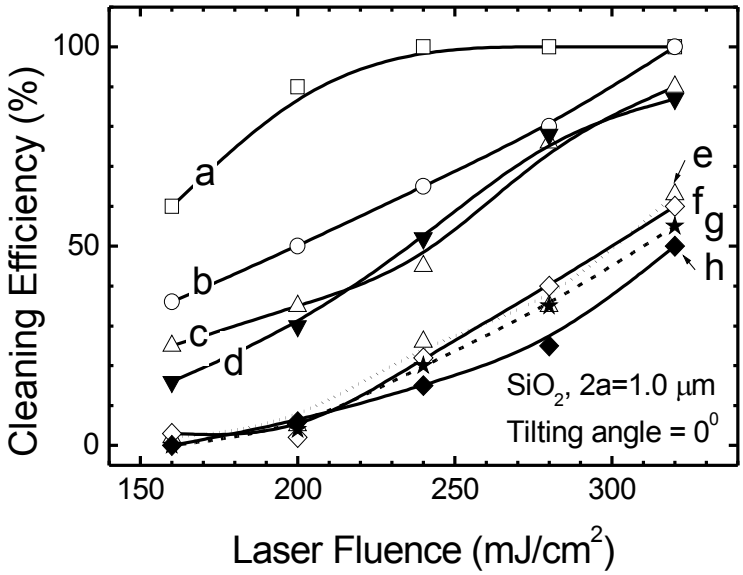

Fig. 38. Cleaning curves for samples with different roughness. The surface roughness increases with the alphabatic order from $\delta = 0$ (a) to $\delta \approx 50$ nm (h). From Zheng, 2001.

see from Figs. 24, that the 1D theory cannot explain experimental results on dry laser cleaning for both small and big particles. It means that some important physics is missing with 1D model. The results of recent papers (Arnold, 2002) do not confirm the 1D thermal expansion mechanism either.

The main idea of our latest examinations was that instead of a 1D model one should use a 3D model, based on the ideas of near field focusing and optical resonance effect, which are very sensitive to wavelength, particle size, incident angle and surface morphology.

Our examinations show, that for transparent spherical particles with a size comparable or even smaller than the laser wavelength, the optical resonance and substrate reflection produce under the particle an "enhanced" near-field light intensity, which may exceed the incident laser intensity by one or two orders of magnitude.

The present work was devoted to the examination of the mentioned 3D effects in theory and experiments. The results can be summarized as follows:

1) The threshold fluence for laser cleaning strongly depends on the particle sizes (smaller particles need higher fluence). This dependence does not follow the law $\Phi_{th} \propto R^{-2}$ (see in Fig. 33)
2) Field enhancement and its consequences play a major role in the dry laser cleaning process. Within the thermal expansion mechanism the near-field focusing should result in strong angular dependence in the cleaning efficiency vs. angle of radiation incidence, which was confirmed experimentally (see in Fig. 37).
3) Rapid decrease in the near field intensity with particle lifting should yield decrease in cleaning efficiency with surface roughness (in spite of decrease in adhesion force vs. roughness). This effect was confirmed experimentally (see in Fig. 38).
4) New peculiarities arise with ultrashort, femtosecond laser pulses. First the enhanced intensity leads to a local ablation of the substrate, which acts as a cleaning mechanism and results in particle ejection via momentum transfer (Mosbacher, 2002a). Second this enhanced intensity is the main source of substrate damage in the dry laser cleaning process.
5) The theory (Luk`yanchuk, 2000) predicts a rapid variation in the cleaning efficiency with a change of wavelength (for fixed size of particles) due to optical resonance effect. To check this prediction experiments with a tunable laser have been carried out, which revealed evidence of optical resonances (Mosbacher, 2002d).

ACKNOWLEDGEMENT

We wish to thank Prof. S. I. Anisimov and Dr. N. Arnold for discussions. B. L. is thankful to Russian Basic Research Foundation (grants 01-02-16136, 01-02-16189). The research at University of Konstanz is supported by the European Union (grant n^{o} ERBFMRXCT98 0188), the Konstanz Center for Modern Optics and Wacker Siltronic, Germany.

References:

Abrikosov A. A., Gorkov L. P., Dzyaloshinski I. E., *Methods of Quantum Field Theory in Statistical Physics*, (Prentice-Hall, Englewood Cliffs, New Jersey, 1965)

Arnold N., Schrems G., Mühlberger T., Bertsch M., Mosbacher M., Leiderer P., Bäuerle D., *Proc. SPIE,* vol. **4426**, pp. 340-346 (2002); see also Chapter 2 in this book

Assendel'ft E. Y., Beklemyshev V. I., Makhonin I. I., et al., *Sov. Tech. Phys. Lett.* **14**, 1006 (1988 a)

Assendel'ft E. Y., Beklemyshev V. I., Makhonin I. I., et al., *Sov. Tech. Phys. Lett.* **14**, 1494 (1988 b)

Barber P. W., Hill S. C., *Light Scattering by Particles: Computational Methods*, (World Scientific, Singapore 1990)

Bäuerle D., *Laser Processing and Chemistry*, 3^{d} ed., (Springer, Berlin, 2000)

Beklemyshev V. I., Makarov V. V., Makhonin I. I., Petrov Yu. N., Prokhorov A. M., Pustovoy V. I., JETP Letters, vol. **46**, 347 (1987)

Bobbert P. A., Vlieger J., *Physica A*, vol. **137**, 209 (1986 a)

Bobbert P. A., Vlieger J., Greef R., *Physica A*, vol. **137**, 243 (1986 b)

Bohren C. E., Huffman D. R., *Absorption and Scattering of Light by Small Particles*, (John Willey & Sons, 1983)

Boneberg J., *Metallische Dünnfilmschmelzen von Halbleiterschichten nach ns-Laser-Annealing*, Hartung Gorre, Konstanz (1993)

Born M., Wolf E., *Principles of Optics*, 7-th Edition, (Cambridge University Press, 1999)

Bowing R. A., In (Mittal, 1988), pp. 129

Boykov D. A., Kolomenskii A. A., Maznev A. A., Maishev Yu. V., Panfilov Yu. V., Ravich A. M., *USSR Patent* #4872125/25 (August, 1991)

Burmeister F., Schäfle C., Keilhofer B., Bechingr C., Boneberg J., Leiderer P., *Adv. Mater.* **10**, 495 (1998).

Derjaguin B. V., *Kolloid Z.*, **69**, 155 (1934)

Derjaguin B. V., Muller V. M., Toporov Yu. P., *Journal of Colloid and Interface Science*, **53**, 314 (1975); **73**, 293 (1980)

Dobler V., Oltra R., Boquillon J. P., Mosbacher M., Boneberg J., Leiderer P., *Appl. Phys. A*, **69**, 335 (1999)

Donovan R. P., Locke B. R., Ensor D. S., In (Mittal, 1988), pp. 43-56

Durig U., Pohl D.-W., Rohner F., *J. Appl. Phys.*, **59**, 3318 (1986)

Dzyaloshinski I. E., Pitaevsky L. P., *JETP*, **9**, 1282 (1959)

Dzyaloshinski I. E., Lifshitz E. M., Pitaevsky L. P., *JETP*, **10**, 161 (1960)

Dzyaloshinski I. E., Lifshitz E. M., Pitaevsky L. P., *JETP*, **10**, 165 (1960)

Engelsberg A. C., *Proc. MRS*, vol. **315**, 255 (1993)

Fields M. H., Popp J., Chang R. K., In "*Progress in Optics*", vol. **41**, Ed. by E. Wolf (Elsevier, 2000)
Grigoriev I. S., Meilikhov E. Z. (Eds.), *Handbook of Physical Quantities*, (CRC Press, Boca Raton, 1997)
Hafner C., *The Generalized Multipole Technique for Computational Electromagnetism* (Artech House, Boston, 1990)
Halfpenny D. R., Kane D., *J. Appl. Phys*., vol. **86**, 6641 (1999)
Hamaker H. C., *Physica*, **4** (10), 1058 (1937)
Heim L. O., Blum J., Preuss M., Butt H. J., *Phys. Rev. Lett*., **83**, 3328 (1999)
Huang S. M., Hong M. H., Luk'yanchuk B. S., Lu Y. F., *Laser assisted nanofabrications on metal surfaces with optical near field effects*, Proc. SPIE, vol. **4760** (2002a)
Huang S. M., Hong M. H., Luk`yanchuk B. S., Zheng Y. W., Song W. D., Lu Y.F., Chong T. C., *Pulsed laser-assisted surface structuring with optical near-field enhanced effects,* J. Appl. Phys., (2002b)
Imen K., Lee S. J., Allen S. D., *Appl. Phys. Lett*., **58**, 203 (1991a)
Imen K., Lee S. J., Allen S. D., *U. S. Patent* Serial No. 4, 987, 286 (January 1991b)
Israelachvili Ya., *Intermolecular and Surface Forces*, 2^{d} ed., (Academic Press, London, 1991)
Johnson K. L., Kendall K., Roberts A. D., *Proc. Roy. Soc*., **A 324**, 301 (1971)
Johnson K. L., In: "*Theoretical and Applied Mechanics*", Ed. by W. T. Koiter, p.133 (North-Holland 1976)
Karlov N. V., Kirichenko N. A., Luk'yanchuk B. S., *Laser Thermochemistry. Fundamentals and Applications,* (Cambridge International Science Publishing, Cambridge, 2000)
Kelley J. D., Hovis F. E., *Microelectronic Engineering* **20**, 159 (1993)
Kerker M., *The scattering of Light*, (Academic Press, New York & London, 1969)
Kerker M., *Selected Papers on Light Scattering*, Proc. SPIE, vol. **951** (Part One), (1989), see Section 4 "*Optical Resonances*"
Klimchitskaya G. L., Mohideen U., Mostepanenko V. M., *Phys. Rev. A*, vol. **61**, 062107 (2000)
Kolomenskii A. A., Maznev A. A., *Sov. Tech. Phys*. Lett., **17**, 62 (1991)
Kurz H., Lompré L. A., Liu J. M., *J. de Physique* **10**, C5 (1983)

Landau L. D., Lifshitz E. M, *Course of Theoretical Physics* (Pergamon Press, 1994, 1998, 1999):
Vol. 1, *Mechanics*, 3rd Edition
Vol. 2, *The Classical Theory of Field*, 4th Edition
Vol. 3, *Quantum Mechanics*, 3rd Edition
Vol. 4, *Quantum Electrodynamics*, 2nd Edition
Vol. 5, *Statistical Physics*, Part 1, 3rd Edition
Vol. 6, *Fluid Mechanics*, 2nd Edition
Vol. 7, *Theory of Elasticity,* 3rd Edition
Vol. 8, *Electrodynamics of Continuous Media*, 2nd Edition
Vol. 9, *Statistical Physics*, Part 2 (see Lifshitz E. M., Pitaevsky L. P.)
Vol. 10, *Physical Kinetics*

Lee L. H., *Fundamentals in Adhesion*, (Plenum Press, New York, 1990)

Leiderer P., Boneberg J., Dobler V., et al, *Proc. SPIE*, vol. **4065**, 249 (2000)

Leontovich M. A., Rytov S. M., *JETP*, **23**, 246 (1952)

Lifshitz E. M., *JETP,* **29**, p. 94 (1955)

Lifshitz E. M., Pitaevsky L. P., *Statistical Physics*, Part 2, §§ 80-82 (Pergamon Press, 1980)

Lowndes D. H., Wood R. F., Westbrook D., *Appl. Phys. Lett.* **43**, 258 (1983)

Lu Y.F., Song W.D., Ang B.W., Chan D.S.H., Low T.S., Appl. Phys. A **65**, 9 (1997)

Lu Y. F., Zheng Y. W., Song W. D., *J. Appl. Phys*. **87**, 1534 (2000a)

Lu Y. F., Song W. D., Luk`yanchuk B. S., Hong M. H., Zheng Y. W., In: "*Laser Solid Interactions for Materials Processing*", Editors: D. Kumar, D. P. Norton, C. B. Lee, K. Ebihara, X. Xi, 2000 MRS Spring Meeting, San Francisco, CA, Vol. **617**, J1.4 (2000b)

Lu Y. F., Zhang L., Song W. D., Zheng Y. W., Luk'yanchuk B. S., *JETP Letters*, vol. **72**, 457 (2000c)

Lu Y. F., Zhang L., Song W. D., Zheng Y. W., Luk'yanchuk B. S., *Proc. SPIE*, vol. **4426**, 143 (2002)

Luk'yanchuk B. S., Zheng Y. W., Lu Y. F., *Proc. SPIE*, vol. **4065**, 576 (2000)

Luk'yanchuk B. S., Zheng Y. W., Lu Y. F., *Proc. SPIE,* vol. **4423**, 115 (2001)

Luk'yanchuk B. S., Zheng Y. W., Lu Y. F., *RIKEN Review*, No. **43**, 37 (2002a)
Luk'yanchuk B. S., Zheng Y. W., Lu Y. F., *Proc. SPIE,* vol. **4426**, 284 (2002b)
Luk'yanchuk B. S., Huang S. M., Hong M. H., *3D effects in dry laser cleaning*, Proc. SPIE, vol. **4760** (2002c)
Madelung O. (Ed.), *Semiconductors-Basic Data*, 2nd Edition, (Springer, Singapore, 1996)
Maugis D., *Journal of Colloid and Interface Science*, **150**, 243 (1992)
Maugis D., Gauthier-Manuel B., *In:* (Rimai D. S., 1995), p. 49
Mishenko M. I., Hovenier J. W., Travis L. D. (Eds.), *Light Scattering by Nonspherical Particles*, (Academic Press, New York, 2000)
Mittal K. L. (Ed.), *Particles on Surfaces: Detection, Adhesion and Removal*, vol. **1** (Plenum Press, New York, NY, 1988)
Mizes H., Loh K. G., Ott M. L., Miller R. J. D., In: "*Particles on Surfaces: Detection, Adhesion and Removal*", Ed. by K. L. Mittal (Marcel Dekker, New York, 1995)
Moody J. E., Hendel R. H., *J. Appl. Phys*., vol. **53**, 4364 (1982)
Morse P. M., Feshbach H., *Methods of Theoretical Physics*, vol. 2 (McGraw-Hill, 1953)
Mosbacher M., Dobler V., Boneberg J., Leiderer P., *Appl. Phys. A* **70**, 669 (2000).
Mosbacher M., Münzer H. -J., Zimmermann J., Solis J., Boneberg J., Leiderer P., *Appl. Phys.* **A 72**, 41 (2001)
Mosbacher M., Bertsch M., Münzer H.-J., Dobler V., Runge B.-U., Bäuerle D., Boneberg J., Leiderer P.: *Proc. SPIE*, vol. **4426**, 308 (2002)
Mosbacher M., Münzer H.-J., Bertsch M., Dobler V., Chaoui N., Siegel J., Oltra R., Bäuerle D., Boneberg J., Leiderer P., In: *„Particles on Surfaces 7: Detection, Adhesion and Removal"*, Ed. by K. L. Mittal, VSP Publishing (2002b, in press).
Mosbacher M., Dobler V., Bertsch M., Münzer H.-J., Boneberg J., Leiderer P., In: *„Particles on Surfaces 8: Detection, Adhesion and Removal"*, Ed. by K. L. Mittal, VSP Publishing (2002c, in press).
Mosbacher M., Dubbers O., Münzer H.-J., Bertsch M., Leiderer P., submitted (2002d)
Muller V. M., Yushchenko V. S., Derjaguin B. V., *Journal of Colloid and Interface Science*, **77**, 91 (1980); **92**, 92 (1983)

Münzer H.-J., Mosbacher M., Bertsch M., Zimmermann J., Leiderer P., Boneberg J., *Journ. Microscopy*, vol. **202**, 129 (2001)
Münzer H.-J., Mosbacher M., Bertsch M., Dubbers O., Burmeister F., Pack A., Wannemacher R., Runge B.-U., Bäuerle D., Boneberg J., Leiderer P., *Proc. SPIE*, vol. **4426**, 180 (2002)
Ordal M. A., Bell R. J., Alexander R. W., Jr., Long L. L., Querry M. R., *Appl. Opts*., **24** (24), 4493(1985)
Osborne-Lee I. W., In (Mittal, 1988), pp. 77
Ozisik M. N., Czisik M. N., *Finite difference methods in heat transfer*, (CRC Press, 1994)
Palik E. D. (Ed.): *Handbook of Optical Constants of Solids*, (Academic Press, Washington, 1985)
Palik E. D. (Ed.): *Handbook of Optical Constants of Solids*, (Academic Press, Boston, 1998)
Prokhorov A. M., Konov V. I., Ursu I., Mihailescu I., *Laser Heating of Metals* (Adam Hilger, Bristol, 1990)
Qiu T. Q., Longtin J. P., Tien C. L., *Journ. of Heat Transfer*, **117**, 340 (1995)
Rimai D. S., DeMejo L. P., Mittal K. L. (Eds.), *Fundamentals of adhesion and interfaces* (Utrecht, VSP Netherlands, 1995)
Rose M. E., *Elementary Theory of Angular Momentum* (Willey, New York, 1957), pp. 48-57
Rytov S. M., *Theory of Electromagnetic Fluctuations and Thermal Radiation*. Publ. of USSR Academy of Sciences, Moscow 1953 (English Translation, AFCRL TR 59-162)
Shaefer D. M., Carpenter M., Gady B., Reifenberger R., Demejo L. P., Rimai D. S., *In:* (Rimai D. S., 1995), p. 35; J. Adhesion Sci. Technol. **9**, 1049 (1995)
Shiles E., Sasaki T., Inokuti M., Smith D. Y., *Phys. Rev. B*, vol. **22**, 1612 (1980)
Sik J., Hora J., Humliche J., *J. Appl. Phys*., vol. **84**, 6291 (1998)
Sokolnikoff I. S., *Mathematical Theory of Elasticity*, 2nd Ed., (McGraw-Hill, 1956)
Soltani M., Ahmadi G., Bayer R. G., Gaynes M. A., J. *Adhesion Sci. Technol.* **9**, 453 (1995)
Stratton J. A., *Electromagnetic Theory*, (McGraw-Hill, New York & London, 1941)

Tam A. C., Leung W. P., Zapka W., Ziemlich W., *J. Appl. Phys.* **71**, 2217 (1992)
Vicanek M., Rosch A., Piron F., Simon G., *Appl. Phys. A*, **59**, 407 (1994)
Visser J., *Advances in Colloid and Interface Science*, **3**, 331 (1972)
Van de Hulst H. C., *Light Scattering by Small Particles*, (Dower Publ., New York, 1981)
Welsh L. P., Tuchman J. A., Herman I. P., *J. Appl. Phys*., **64**, 6274 (1988)
Whitehouse D. J., Archard J. F., Proc. Roy. Soc. **A 310**, 97 (1970).
Wojcik G. L., Vaughan D. K., Galbraith L. K., *Proc. SPIE*, vol. **777**, 21 (1987)
Wolfram S., *Mathematica*, 4th Ed., (Wolfram Media/Cambridge University Press, 1999)
Ye H., Sun C. Q., Huang H., Hing P., *Appl. Phys. Lett*., Vol. **78**, No. 13, 1826 (2001)
Zapka W., Asch K., Meissner K., *European Patent* EP 0297506 A2, 4 January 1989
Zapka W., Ziemlich W., Tam A. C., *Appl. Phys. Lett*., **58**, 2217 (1991a)
Zapka W., Tam A. C., Ziemlich W., *Microelectronics Eng.*., **13**, 547 (1991b)
Zheng J., In *7th Annual Review of Progress in Applied Computational Electromagnetics (ACES)*, Conference Proceedings, Monterrey, pp. 170-173 (1990)
Zheng Y. W., Lu Y. F., Mai Z. H., Song W. D., *Jpn. J. Appl. Phys*., vol. **39**, Part 1, 5894 (2000)
Zheng Y. W., Luk'yanchuk B. S., Lu Y. F., Song W. D., Mai Z. H., *J. Appl. Phys*., vol. **90**, 2135 (2001)